Title

Mechanisms of nuclear content loading to exosomes

Journal

Science Advances, 5(11)

ISSN

2375-2548

Authors

Yokoi, Akira
Villar-Prados, Alejandro
Oliphint, Paul Allen
et al.

Publication Date

2019-11-01

DOI

10.1126/sciadv.aax8849

Peer reviewed

CELL BIOLOGY

Mechanisms of nuclear content loading to exosomes

Akira Yokoi[1]*, Alejandro Villar-Prados[1,2]*, Paul Allen Oliphint[3], Jianhua Zhang[4], Xingzhi Song[4], Peter De Hoff[5], Robert Morey[5,6], Jinsong Liu[7], Jason Roszik[4,8], Karen Clise-Dwyer[9], Jared K. Burks[10], Theresa J. O'Halloran[3], Louise C. Laurent[5,6], Anil K. Sood[1,11]†

Exosome cargoes are highly varied and include proteins, small RNAs, and genomic DNA (gDNA). The presence of gDNA suggests that different intracellular compartments contribute to exosome loading, resulting in distinct exosome subpopulations. However, the loading of gDNA and other nuclear contents into exosomes (nExo) remains poorly understood. Here, we identify the relationship between cancer cell micronuclei (MN), which are markers of genomic instability, and nExo formation. Imaging flow cytometry analyses reveal that 10% of exosomes derived from cancer cells and <1% of exosomes derived from blood and ascites from patients with ovarian cancer carry nuclear contents. Treatment with genotoxic drugs resulted in increased MN and nExos both in vitro and in vivo. We observed that multivesicular body precursors and exosomal markers, such as the tetraspanins, directly interact with MN. Collectively, this work provides new insights related to nExos, which have implications for cancer biomarker development.

INTRODUCTION

Exosomes are small extracellular vesicles that mediate biological and cellular functions including cell-to-cell communication (*1*). Exosomes are generated in early endosomes and then stored in multivesicular bodies (MVBs) that fuse with the plasma membrane and release the exosomes to the extracellular space (*2*). Tetraspanins, proteins known as major exosomal markers, that localize to endosomes, MVBs, and exosomes are thought to be responsible for trafficking cargo into these organelles (*3*). The ability of exosomes to induce distinct biological behaviors in either the cells that secrete them or the recipient cells depends on their cargo (*4*). Exosome cargoes are variable and can include proteins and RNA species (*5*). The presence and abundance of protein and RNA, including microRNAs, can influence cell behavior in several contexts, ranging from immune system activation to suppression of solid tumor growth and cancer metastasis (*6*).

Recent studies have demonstrated the presence of genomic DNA (gDNA) and nuclear proteins within exosomes (*7*). The presence of gDNA in exosomes has been associated with processes such as cell senescence and stimulation of the cGAS/STING inflammatory pathway (*8*). In addition, gDNA is predominantly detected in exosomes derived from cancer cells rather than healthy cells. Paradoxically, gDNA is mainly confined to the cell nucleus and does not normally interact with the cytoplasmic MVBs that give rise to exosomes (*9*). Thus, the mechanisms by which nuclear components are present in exosomes remain poorly understood.

One possibility involves micronuclei (MN), which are cytoplasmic structures enveloped by a nuclear membrane and are generated when the cell nucleus fails to properly segregate nuclear material, including chromosomes. (*10*). This mis-segregation can arise during mitosis and can be driven by DNA-damaging agents, such as radiation, which can result in chromosome fragmentation (*11*). The presence of MN serves as a surrogate marker of genomic instability, which is a hallmark of cancer (*12*). The nuclear envelope that surrounds MN is highly unstable, eventually breaking down and exposing its contents to the cytoplasm during cell division (*13*). Induction of MN formation can promote activation of the cGAS/STING pathway, resulting in an inflammatory response against both senescent and cancer cells (*14*).

Here, we identify a previously unidentified interaction between MN and nExo. We show that induction of MN formation using genotoxic drugs promotes nExo release. Our results suggest a mechanism for the origin of gDNA in exosomes whereby, following MN collapse, their nuclear contents are shuttled into MVBs via tetraspanins. Moreover, we found that exosomal gDNAs in ovarian cancer patients reflect copy number variation (CNV) status of the primary tumor, revealing informative DNA mutations. Thus, nExos can serve as important biomarkers for cancer detection and longitudinal monitoring of cancer patients.

RESULTS

Ovarian cancer exosomes contain nuclear content

Despite the prevalence of gDNA in cancer-derived exosomes, the relationship between genomic instability and the abundance of nExo has not been elucidated. To address this problem, we screened The Cancer Genome Atlas (TCGA) to determine which tumor types have the highest number of chromosomal duplications and are thus the most genomically unstable (Fig. 1A). Of the 25 tumor types investigated, we observed that high-grade serous ovarian cancer (HGSC) ranked fourth highest in median ploidy and the genome was characterized as highly unstable, which has been associated with poor clinical outcomes (*15*).

[1]Department of Gynecologic Oncology and Reproductive Medicine, University of Texas MD Anderson Cancer Center, Houston, TX, USA. [2]Department of Medicine, Stanford University, Stanford, CA, USA. [3]Department of Molecular Biosciences and Institute for Cellular and Molecular Biology, University of Texas at Austin, Austin, TX, USA. [4]Department of Genomic Medicine, University of Texas MD Anderson Cancer Center, Houston, TX, USA. [5]Department of Obstetrics, Gynecology, and Reproductive Sciences, University of California, San Diego, La Jolla, CA, USA. [6]Bioinformatics and Systems Biology Graduate Program, University of California, San Diego, La Jolla, CA, USA. [7]Department of Pathology, University of Texas MD Anderson Cancer Center, Houston, TX, USA. [8]Department of Melanoma Medical Oncology, University of Texas MD Anderson Cancer Center, Houston, TX, USA. [9]Section of Transplant Immunology, Department of Stem Cell Transplantation and Cellular Therapy, University of Texas MD Anderson Cancer Center, Houston, TX, USA. [10]Department of Leukemia and Division of Cancer Medicine, University of Texas MD Anderson Cancer Center, Houston, TX, USA. [11]Center for RNA Interference and Non-Coding RNA, University of Texas MD Anderson Cancer Center, Houston, TX, USA.
*These authors contributed equally to this work.
†Corresponding author. Email: asood@mdanderson.org

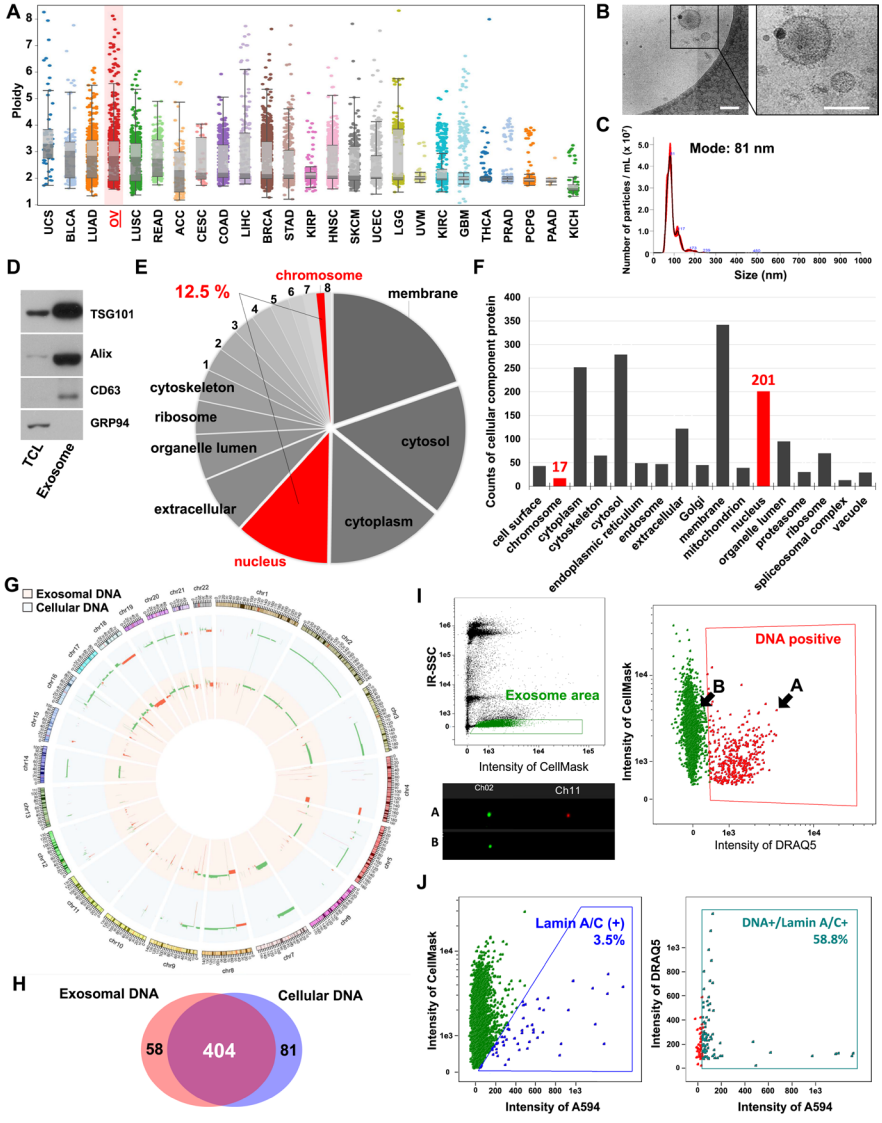

Fig. 1. Characterization of nuclear-derived content from ovarian cancer exosomes. (**A**) TCGA pan-cancer ploidy analysis of 20 cancer types. $n = 62$ [kidney chromophobe (KICH)], $n = 418$ [brain low-grade glioma (LGG)], $n = 7$ [pancreatic cancer (PAAD)], $n = 138$ [pheochromocytoma (PCPG)], $n = 353$ [prostate adenocarcinoma (PRAD)], $n = 184$ [thyroid carcinoma (THCA)], $n = 543$ [glioblastoma (GBM)], $n = 415$ [kidney clear cell carcinoma (KIRC)], $n = 61$ [uveal melanoma (UVM)], $n = 415$ [uterine endometrial carcinoma (UCEC)], $n = 257$ [skin cutaneous melanoma (SKCM)], $n = 501$ [head and neck squamous carcinoma (HNSC)], $n = 155$ [kidney papillary carcinoma (KIRP)], $n = 330$ [stomach adenocarcinoma (STAD)], $n = 940$ [breast cancer (BRCA)], $n = 187$ [liver hepatocellular carcinoma (LIHC)], $n = 396$ [colon adenocarcinoma (COAD)], $n = 34$ [cervical cancer (CESC)], $n = 85$ [adrenocortical carcinoma (ACC)], $n = 158$ [renal adenocarcinoma (READ)], $n = 435$ [lung squamous carcinoma (LUSC)], $n = 544$ [ovarian cancer (OV)], $n = 429$ [lung adenocarcinoma (LUAD)], $n = 144$ [bladder cancer (BLCA)], and $n = 55$ [uterine carcinosarcoma (UCS)]. (**B**) Cryo-EM image of the exosomes isolated from OVCAR-5 cells. Scale bars, 100 nm. (**C**) NTA for the exosomes isolated from OVCAR-5 cells. (**D**) Western blot analysis of exosome markers in OVCAR-5. TSG101, Alix, and CD63 are used as exosome markers, and GRP94 is used as a marker of cellular contamination. TCL, total cell lysate. (**E**) Pie chart of cellular compartment proteins resulting from MS analysis in OVCAR-5 cell–derived exosomes. Nuclear components are highlighted in red: 1, endoplasmic reticulum; 2, endosome; 3, Golgi; 4, cell surface; 5, mitochondrion; 6, proteasome; 7, vacuole; 8, spliceosomal complex. (**F**) Counts of the cellular compartment origin of proteins resulting from MS analysis in OVCAR-5 cell–derived exosomes. The *x* axis represents the categories of cellular compartments. Nuclear proteins identified in chromosome and nucleus are highlighted in red. (**G**) CNVs of both the exosomal DNA (inner red circle) and cellular DNA (outer blue circle), both derived from OVCAR-5 cells, are displayed on a chromosome map generated using Circos (v0.69.3). The outermost circle represents human chromosomes with coordinates (megabases). The green and red histograms inside the blue and red inner circles represent copy number alterations identified by cnvkit. The larger the bar on the track, the larger the copy number alteration (log scale). Green bars represent amplification events, and red bars represent deletions. (**H**) A Venn diagram of all the CNVs overlapping between the exosomal and cellular DNA derived from OVCAR-5 cells. (**I**) Representative plots of OVCAR-5 exosomes from flow cytometry analysis. Top left: Particles are shown as black dots, and exosomes are in the green area. Right: Each dot indicates single exosomes stained with CellMask Green (Ch02), and the red gate indicates DNA-positive particles stained with DRAQ5 (Ch11). Bottom left: Snapshots of individually stained exosomes. (A) and (B) are the exosomes present in the areas indicated in the right panel. (A) represents the DNA-positive exosomes, and (B) represents the negative exosomes. (**J**) Representative gate images of OVCAR-5 exosomes from imaging flow cytometry analysis. Left: Each green dot indicates a single exosome, and the blue gate indicates a Lamin A/C–positive population. Right: All dots are from DNA-positive exosomes, and the green gate indicates a Lamin A/C–positive population.

Using HGSC preclinical models, we first tested the purity of our exosome isolation approach with cryo–electron microscopy (cryo-EM), nanoparticle tracking analysis (NTA), and immunoblotting assays (Fig. 1, B to D, and fig. S1, A to C). To determine whether the exosomes carried nuclear proteins, we performed a mass spectrometry (MS) analysis on the exosomal fractions. In the exosomes isolated from OVCAR-5 (OVCAR-5exo) cells, an HGSC cell line, 201 nuclei-associated proteins and 17 chromosome-associated proteins were detected, and 12.5% of the total number of detected proteins were nuclear-derived (Fig. 1, E and F).

On the basis of these findings, we next used whole-genome sequencing (WGS) to compare CNV between the DNA from OVCAR-5 cells and exosomes (Fig. 1G). The CNVs were quite similar between the cell and exosome DNA (Fig. 1H). While some studies have shown that gDNA is present in exosomes (*7*, *9*), the subpopulation of exosomes that contain DNA and the amount of exosomes that contain DNA are unclear. To address this question, we used the Amnis Image Stream X, MkII flow cytometer, which can detect single exosomes as previously described (*16*). We adapted this methodology to analyze nExo by first staining our exosomes with the CellMask plasma membrane stain and loading onto the flow analyzer. Beads of various sizes were used as reference to set the gates for the exosome population (Fig. 1I, left upper panel, and fig. S1, D to F). The particles with a side-scatter (SSC) aspect ratio close to 1 were specifically selected to exclude exosome aggregates from our analysis (fig. S1G). To confirm that the particles detected were bound by lipid membranes, exosomes were treated with 0.5% NP-40 to disrupt the membrane. This almost completely abolished the presence of detected exosomes (fig. S1H). Furthermore, exosome concentration positively correlated (R^2 = 0.968) with the particles detected by the analyzer (fig. S1I). These results demonstrate the successful detection of exosomes by our imaging flow cytometry method. In addition, we confirmed that this method can be used for exosome analysis without the procedure of exosome isolation because it detected exosomes by using cell culture medium (fig. S1J).

To identify the presence of gDNA and to quantify the percentage of DNA-positive exosomes, the exosomes were stained with DRAQ5, a dye that preferentially binds double-stranded DNA (dsDNA) and is cell permeant to allow quantification of the percentage of DNA-positive exosomes (Fig. 1I). In addition, our single-particle imaging flow cytometry method allowed quantification of subpopulations of DNA-positive exosomes that were also positive for other exosome protein markers, such as tetraspanins (Fig. 1I and fig. S2A). CD9 and CD63, well-documented exosome markers, were abundantly detected in both DNA-positive and DNA-negative exosomes (fig. S2A). To confirm the intra-exosomal localization of DNA, exosomes were treated with deoxyribonuclease (DNase) I to degrade DNA attached to the outer membrane of exosomes. There was approximately a 50% reduction in DNA-positive exosomes after DNase I treatment (fig. S2B). These results suggest that gDNA is present on both the surface and the inside of exosomes. In addition to gDNA, we also tested exosomes for the presence of Lamin A/C, a nuclear envelope protein that was present in our OVCAR5-exo MS data (Fig. 1, E and F). We observed that Lamin A/C was also detectable by flow cytometry (Fig. 1J). This result was further validated by detection of Lamin A/C from isolated exosomes via Western blot (fig. S2C). Contrary to gDNA, Lamin A/C was not as abundant in OVACR5-exo, but we did observe that more than 50% of DNA-positive exosomes were also positive for Lamin A/C (Fig. 1J and fig. S2D). Other nuclear proteins, such as importin, Nesprin-2, and Lamin B1, were also detected in DNA-positive exosomes via flow cytometry in OVCAR5-exo, but their abundance was more variable (fig. S2E).

Induction of MN increases the population of DNA-carrying exosomes

Similar to the presence of gDNA in cancer-derived exosomes, MN are also more prevalent in cancer cells due to their inherent genomic instability (*10*). On the basis of this idea, we investigated whether any relationship existed between the presence of MN and nExo. We first determined the baseline number of cells containing MN in primary healthy fallopian tube epithelial (FTE) cells compared to ovarian cancer cell lines. In primary FTE cells, considered to be the cell of origin for many HGSCs (*17*), the prevalence of MN-containing cells was 1% (Fig. 2, A and B). In contrast, about 4% of ovarian cancer cells contained MN (Fig. 2, A and B). Comparing the amount of nExo secreted by healthy and cancerous cells, we found that cancer cells secreted a significantly higher population of nExo (FTEexo, 0.12 ± 0.04%; OVCAR-5exo, 8.26 ± 1.62%; and OVCAR-8exo, 8.25 ± 2.61%) (Fig. 2, C and D). These data suggest that cells with high genomic instability and therefore increased MN, such as cancer cells, secrete a larger number of nExos.

To further test our hypothesis, we treated ovarian cancer cells with the genotoxic drugs topotecan (10 nM) or olaparib (20 μM) to induce the formation of MN. Upon treatment with either drug, the number of MN increased significantly (Fig. 2, E and F, and fig. S3A). Similarly, the population of exosomes containing gDNA (Fig. 2, G and H, and fig. S3, B and C) and nuclear proteins (fig. S3D) was also increased after treatment with these drugs. These results indicate that inducing genomic instability increases MN production and subsequently increases nExo abundance.

To validate these findings in vivo, we used the OVCAR-5 ovarian cancer model, which represents disseminated peritoneal disease. As shown in the schematic diagram (Fig. 3A), each tumor-bearing mouse was treated with the maximum tolerated dose of topotecan (7.5 mg/kg) and euthanized 48 hours later (*18*). Tumor growth in each mouse was confirmed by in vivo imaging (Fig. 3B). To determine whether topotecan could induce MN formation, as we observed in vitro, tumor nodules were harvested, sectioned, and stained with hematoxylin and eosin (H&E) and examined via bright light and by immunofluorescence (IF) microscopy (Fig. 3, C and D). H&E staining confirmed the presence of MN after topotecan treatment (Fig. 3C). To calculate the number of MN, multiple IF images of tumor slides were taken, and MN were systematically counted by the Vectra–inForm Image Analysis System (PerkinElmer) (Fig. 3D). There was a trend toward increased MN-positive cell percentages in the topotecan-treated group versus vehicle control, although this percentage was not statistically significant (Fig. 3E).

To measure differences in the amount of nExos produced after each treatment, exosomes were isolated from serum and ascites of tumor-bearing mice from each group, and their purity was confirmed by cryo-EM, NTA, and Western blotting for CD63 (Fig. 3, F to H) and quantified by imaging flow cytometry. Tumor-bearing mice generally had significantly more nExos in their serum than did the non–tumor-bearing mice (P = 0.008) (Fig. 3I). Comparing topotecan-treated mice with vehicle control, we observed a significant increase of nExos in ascites (P = 0.028) but no difference in the serum nExos (Fig. 3, J and K). These results indicate that tumors produce more

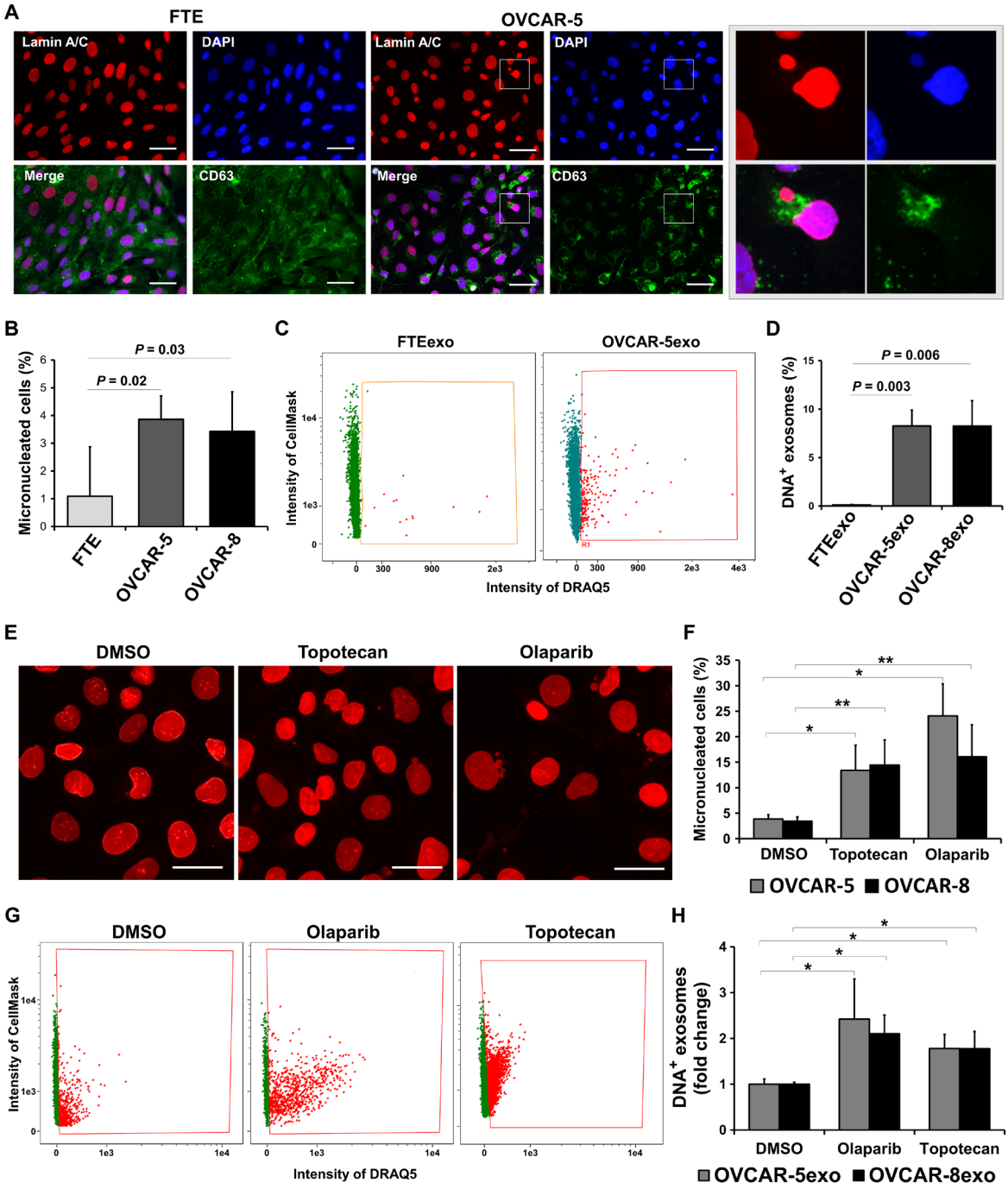

Fig. 2. Promoting MN formation increases DNA-carrying exosomes. (**A**) Immunofluorescence (IF) images of FTE and OVCAR-5 cells. The inset shows a magnified image of a micronucleated OVCAR-5 cell in the right panel. Scale bars, 50 μm. (**B**) Quantification of MN cells in FTE, OVCAR-5, and OVCAR-8 cells. MN counting is described in Materials and Methods. The experiment was performed in three independent biological replicates, and the average of the fold changes was calculated. Error bars are represented as SD. Statistical significance was determined by conducting an unpaired Student's *t* test. (**C**) Representative images of FTEexo and OVCAR-5exo from imaging flow cytometry analysis. The gates in both graphs indicate the DNA-positive population. (**D**) Population of DNA-positive exosomes in FTEexo, OVCAR-5exo, and OVCAR-8exo. The experiment was performed in three independent biological replicates, and the average of the fold changes was calculated. Error bars represent SD. Statistical significance was determined by conducting an unpaired Student's *t* test. (**E**) Representative images of nuclei from OVCAR-5 cells. Nuclei were IF-stained with Lamin A/C antibody. Scale bars, 50 μm. (**F**) Quantification of MN cells in OVCAR-5 and OVCAR-8 cells treated with DMSO, topotecan, and olaparib. The experiment was performed in three independent biological replicates, and the average of fold changes was calculated. Error bars represent SD. Statistical significance was determined by conducting an unpaired Student's *t* test. $^{*}P < 0.05$, $^{**}P < 0.01$. (**G**) Representative images of OVCAR-5exo in imaging flow cytometry analysis. (**H**) Population of DNA-positive exosomes in OVCAR-5exo and OVCAR-8exo. Parental cells were treated with DMSO, olaparib, or topotecan for 48 hours. FTEexo, OVCAR-5exo, and OVCAR-8exo indicate exosomes derived from FTE, OVCAR-5, and OVCAR-8 cells, respectively. The experiment was performed in three independent biological replicates, and the average of fold changes was calculated. Error bars represent SD. Statistical significance was determined by conducting an unpaired Student's *t* test. $^{*}P < 0.05$.

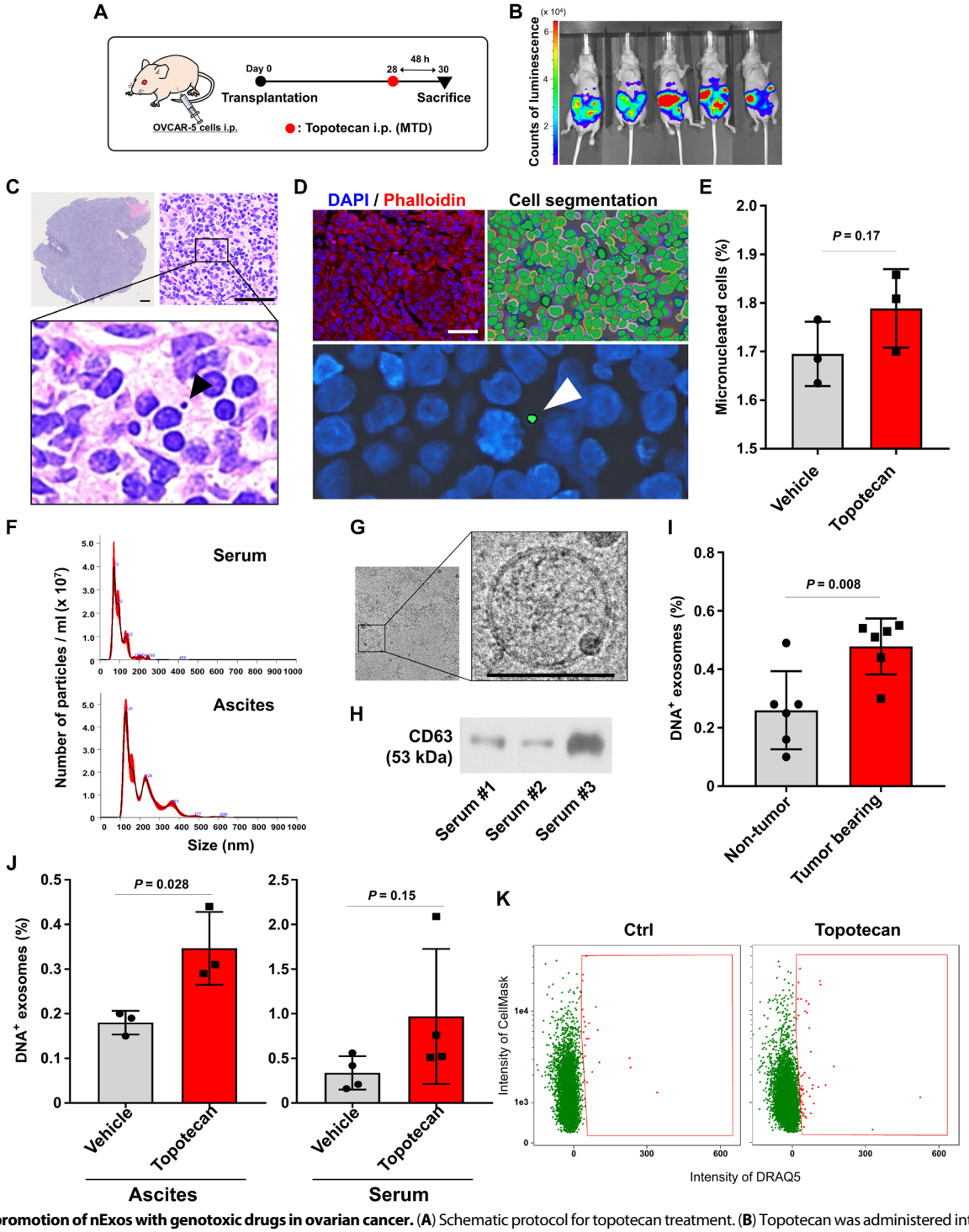

Fig. 3. In vivo promotion of nExos with genotoxic drugs in ovarian cancer. (**A**) Schematic protocol for topotecan treatment. (**B**) Topotecan was administered intraperitoneally. All mice were euthanized on day 30. *n* of vehicle control–treated mice = 4 and *n* of topotecan-treated mice = 4. (**C**) Representative image of tumor tissue sections stained with hematoxylin and eosin (H&E). Scale bars, 700 μm (left panel) and 100 μm (middle panel). Black arrowhead indicates MN. (**D**) Left upper panel: Representative image of tumor tissue stained with DAPI and phalloidin. Scale bar, 50 μm. Right upper panel: Representative image of cell segmentation with Vectra imaging software. Lower panel: Representative image of the detected MN, indicated by white arrowhead. (**E**) Quantification of MN cells. MN counting is described in Materials and Methods. *n* of vehicle control–treated mice = 3 and *n* of topotecan-treated mice = 3. Error bars represent SD. Statistical significance was determined by conducting an unpaired Student's *t* test. (**F**) Nanoparticle tracking analyses for exosomes derived from plasma and ascites. (**G**) Representative cryo-EM images of ascites exosomes from OVCAR-5 intraperitoneal model. Scale bar, 100 nm. (**H**) Western blot of mouse plasma exosomes (*n* = 3). (**I**) Population of DNA-positive exosomes in serum from non–tumor-bearing mouse and OVCAR-5 intraperitoneal model. *n* = each 6. Error bars represent SD. Statistical significance was determined by conducting unpaired Student's *t* test. (**J**) Population of DNA-positive exosomes in serum and ascites from the mice treated with topotecan or vehicle. *n* = ascites, each 3 and serum, each 4. Error bars represent SD. Statistical significance was determined by conducting unpaired Student's *t* test. (**K**) Representative images of serum exosome in imaging flow cytometry analysis.

nExos and that genotoxic drugs promote MN formation in vivo, increasing the amount of nExo release.

MN and nExo share content and interact in live cells

We next compared the relative nuclear protein abundance between MN and nExos. MN from OVCAR-5 cells were isolated via sucrose gradient ultracentrifugation, and fractions enriched for MN were washed and submitted for MS (Fig. 4A) (*19*). MN enrichment was confirmed with 4′,6-diamidino-2-phenylindole (DAPI) staining and IF (Fig. 4A). MS analysis of the MN fraction revealed substantial similarity between OVCAR-5 MN and nExo protein content, with 127 proteins overlapping between the two cellular compartments (Fig. 4, B and C). Some of these shared nuclear proteins included Lamin A/C and Histone H2B as well as some exosome markers such as heat shock proteins (Fig. 4C).

Next, we determined whether MN and exosome-associated proteins interact within cells. Confocal imaging of exosome markers such as CD63, CD9, and CD81 revealed colocalization of these proteins either in the nuclear envelope or inside the MN of ovarian cancer cells (Fig. 4, D and E, and fig. S4A). To further explore whether this interaction occurred in live cells, we carried out time-lapse imaging of cells overexpressing fluorescently tagged nuclear proteins and tetraspanins. Both CD9 and CD63 actively interacted with MN in OVCAR-5 cells (Fig. 4, F and G, and movies S1 and S2). These findings suggest that both MN and nExos share a high degree of nuclear content and that these structures actively interact within living cells.

Cargo of disrupted MN is loaded into exosomes

The envelope of MN is known to be unstable, and upon its collapse, MN contents including gDNA are exposed to the cell cytoplasm (*13*). Therefore, we asked whether this collapse can induce the loading of MN contents into exosomes. Consistent with previous findings, confocal imaging of ovarian cancer cells showed that some MN were not surrounded by their nuclear envelope, suggesting MN collapse (Fig. 5, A and B, and fig. S4B). Of interest, we observed that tetraspanin proteins, which can serve as markers for MVBs, often surrounded the MN with either partial or total nuclear envelope collapse (Fig. 5, A and B). These results were verified by transmission electron microscopy (TEM) (Fig. 5, C to E). This revealed that, similar to our confocal observations, ovarian cancer cells contained collapsed MN (Fig. 5C and fig. S4C).

To address the mechanism behind nuclear content loading into exosomes, we hypothesized that collapsing MN directly interact with the molecular machinery for exosome biosynthesis. Exosomes are initially formed from the intraluminal vesicles of early endosomes and are then stored in MVBs (*2*). These vesicles are then released as exosomes to the extracellular space by fusion of MVBs with the plasma membrane (*2*). TEM revealed that MVBs were located near MN and early endosomes, and thus could directly interact with collapsing MN (Fig. 5, D and E). Further, confocal analysis showed that intact and collapsed MN were both positive for EEA1, the early endosome marker (Fig. 5F and fig. S4D). However, a recent report indicates that extracellular DNA can be secreted outside of the exosomal pathway via amphisomes (*20*). In accordance with this, we found that MN also contained LC3B, an amphisome and autophagosome marker, revealed by immunostaining (fig. S4E). In contrast, MN contained less LMAP-1, the late endosome/lysosome marker, compared to EEA1 and LC3B (fig. S4E). These results suggest that gDNA can be secreted in an exosome-dependent or exosome-independent manner, in which collapsing MN can interact with either early endosomes or amphisomes.

To further explore the molecular mechanism driving MN content loading into exosomes, we focused on tetraspanins, such as CD63, as they are involved in exosome/MVB cargo loading (*3*). To determine whether tetraspanins are necessary for loading MN content into the endosomes and ultimately into nExos, we knocked down CD63 in ovarian cancer cell lines with short hairpin RNA (shRNA). After confirmation of CD63 protein knockdown (Fig. 5G), we examined changes in the number of nExos by flow cytometry. Cells with CD63 knockdown secreted fewer nExos than control cells (Fig. 5H), indicating that CD63 plays an important role in loading nuclear content into nExos. To further explore the role of CD63 in nExo loading, immunoprecipitation (IP) experiments were performed. CD63 pulldown from OVCAR-5 cell lysates revealed an association with DNA and Histone H2B (Fig. 5, I and J). Thus, CD63 can create a complex of gDNA and nuclear proteins and may be important for DNA loading in exosomes.

Detection of nExo in clinical samples

To explore the clinical relevance of nExo, we isolated exosomes from the plasma and ascites of patients with HGSC to characterize their exosomal contents (Fig. 6, A and B). Because of the abundant immunoglobulin contamination present in exosomes isolated by ultracentrifugation from human serum, we purified these exosomes using size exclusion chromatography and then performed MS proteomic analysis (*21*). MS analysis demonstrated that, of the total proteins identified in patient-derived exosomes, 3.2 to 3.6% were nuclear proteins (Fig. 6, C and D, and fig. S5, A to E). MN were also detected in human tumor tissues, with a prevalence of 1% micronucleated cells per tumor analyzed (Fig. 6, E and F, and fig. S5F). Using flow cytometry, <1% of exosomes contained gDNA, which was consistent with our in vivo mouse model data (Fig. 3I and fig. S5G).

WGS analysis of advanced-stage HGSC patient samples revealed that 43 gene mutations were found in both tumor and nExos derived from ascites. Several of these mutated genes are involved in DNA repair, e.g., *DROSHA*, *LIG4*, *MACROD2*, *SATB1*, *RASSF6*, and *BIRC2* (Fig. 6H) (*22*–*27*). In addition, based on the result of read counts, the vast majority of DNA in exosomes was genomic in origin rather than mitochondrial, and the mutation signature was similar (Fig. 6I and fig. S6A). Moreover, ascites exosomes have a CNV similar to the primary tumor, but plasma exosomes did not (Fig. 6J and fig. S6, B to D).

DISCUSSION

In this study, we identified and characterized a subpopulation of nExos and provided mechanistic insights into the packaging of their nuclear content. Our imaging flow cytometry–based method allowed accurate quantification of the nExo subpopulation both in vivo and in vitro. We identified a link between MN formation and the generation of nExos upon induction of genomic instability with genotoxic drugs. In addition, our results suggest that MN collapse serves as a source of nuclear content shuttled into MVB via tetraspanins (fig. S7). Last, we identified the presence of MN and nExos in the ascites of patients with ovarian cancer, which holds promise for rapid assessment of the genomic status of those tumors.

The identification of a nExo subpopulation in preclinical and clinical samples is one of the most important findings in this study. To our knowledge, this is the first report to quantify this population of exosomes using imaging flow cytometry. As described above, cancer cells secrete more nExo than normal cells. However, <1% of

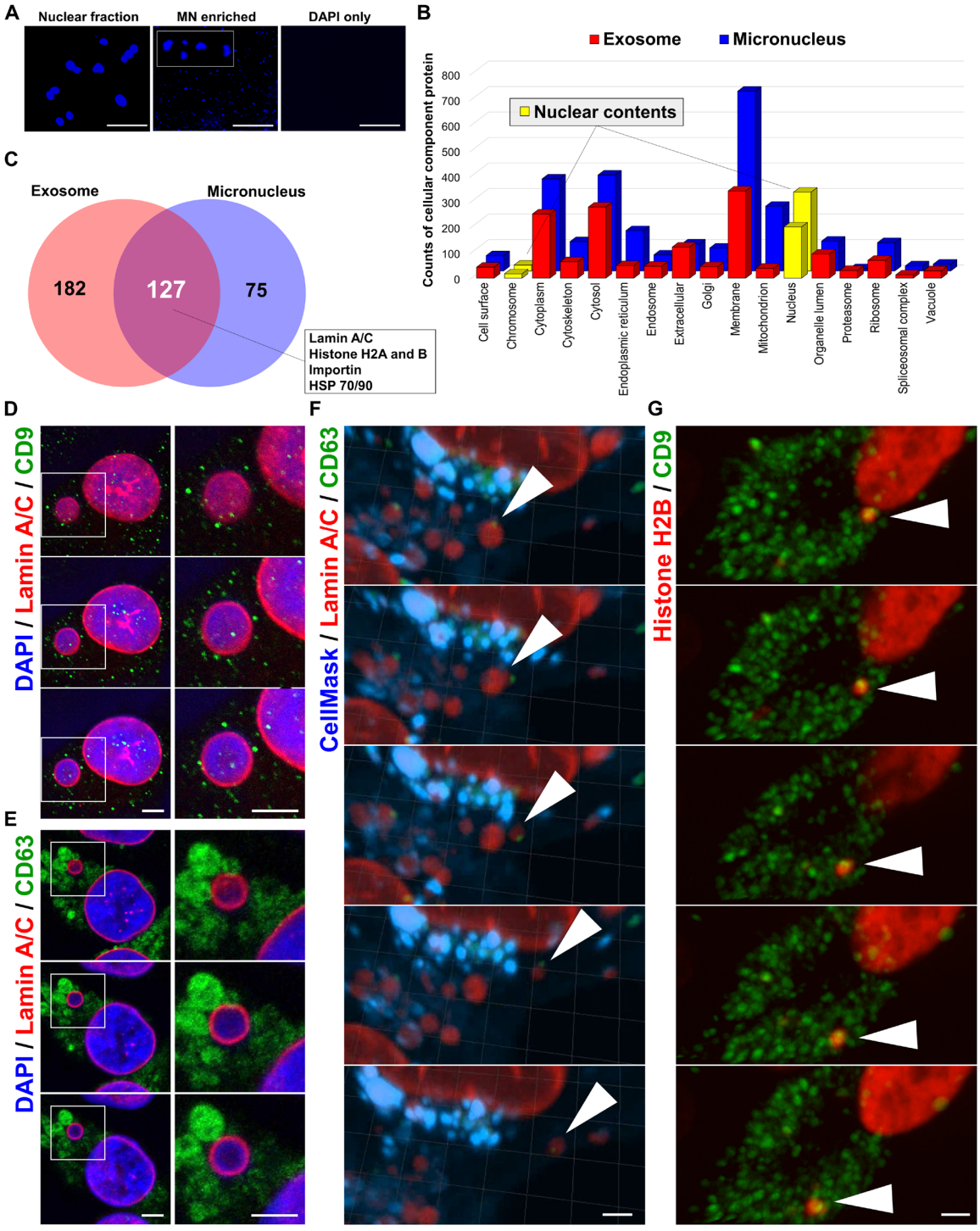

Fig. 4. MN and nExo contain similar protein content. (**A**) Representative images of nuclear fraction and MN-enriched fraction. All samples were obtained from OVCAR-5 cells and stained with DAPI. The white box in the middle image is a magnified view. Scale bar, 50 μm. (**B**) Counts of protein cellular compartment of origin resulting from MS analysis in exosome and MN-enriched fraction. Samples were obtained from OVCAR-5 cells. The *x* axis represents the categories of cell components. Proteins from nuclear and chromosome compartments highlighted in yellow. (**C**) Venn diagram showing overlapping proteins between exosome and MN-enriched fraction. Samples were obtained from OVCAR-5 cells. Lamin A/C, Histone H2A/B, importin, and heat shock protein (HSP) 70/90 were included in the overlapped 127 proteins. (**D** and **E**) Serial confocal images of mCherry-LaminA/C–expressing OVCAR-5 cells. Nuclei were stained with DAPI. CD63 and CD9 were IF-stained with antibodies as described in Materials and Methods. Scale bars, 5 μm. (**F**) Representative images from time-lapse imaging in mCherry-LaminA/C–expressing OVCAR-5 cells. Cell membrane was stained with CellMask Deep Red. Cells stably expressed green fluorescent protein (GFP)–CD63 by lentiviral infections as described in Materials and Methods. Scale bar, 3 μm. (**G**) Representative images of time-lapse imaging in mCherry-Histone H2B–expressing OVCAR-5 cells. Cells were transiently transfected with mEmerald-CD9 plasmid as described in Materials and Methods. Scale bar, 4 μm.

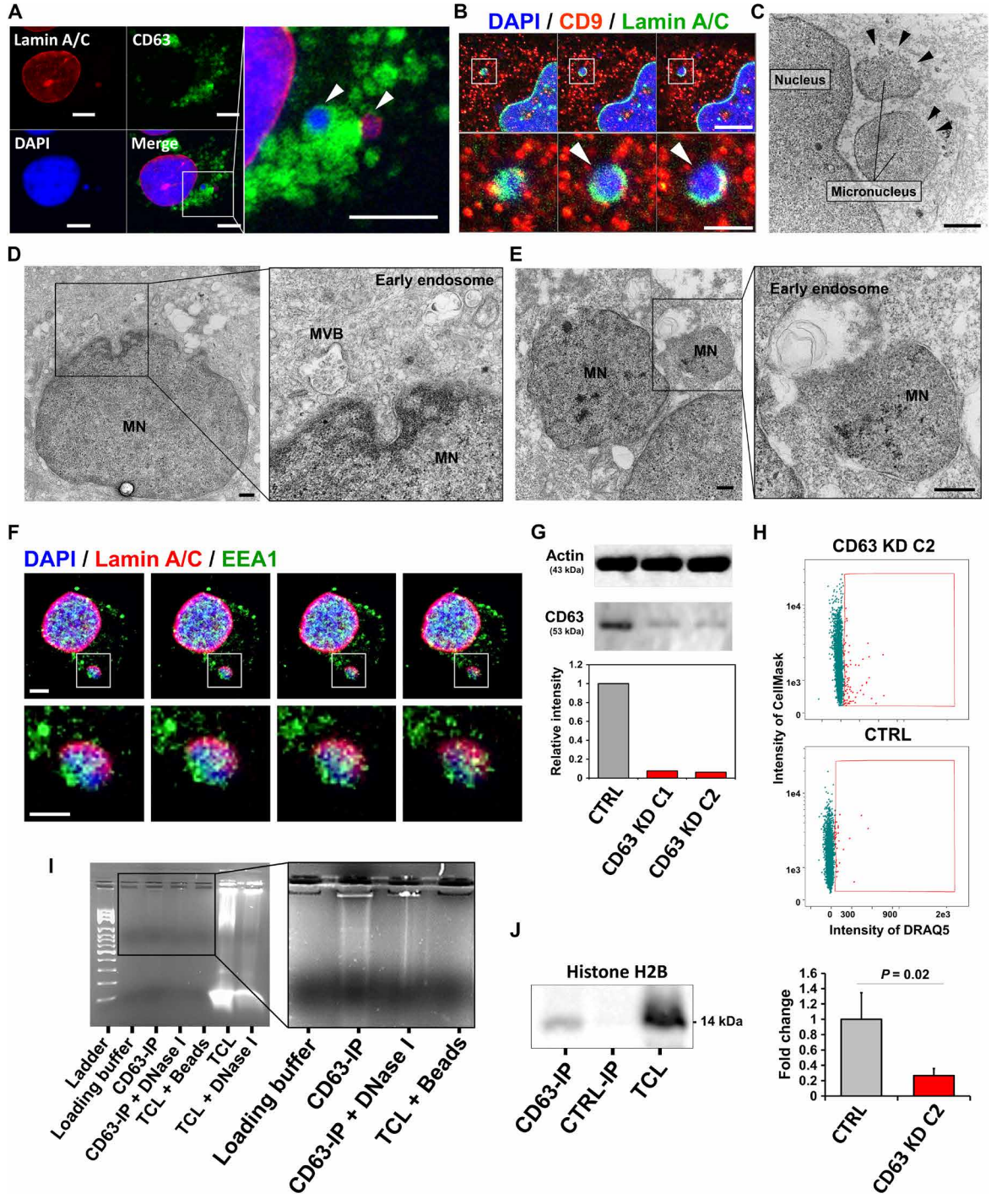

Fig. 5. Cargo of disrupted MN is loaded into nExos. (**A**) Confocal image of OVCAR-5 cells. Nuclei were stained with DAPI, and Lamin A/C and CD63 were IF-stained as described in Materials and Methods. Scale bars, 5 μm. (**B**) Serial confocal stack images of OVCAR-5 cells. Nuclei were stained with DAPI, and Lamin A/C and CD9 were IF-stained with antibodies as described in Materials and Methods. Scale bars, 10 μm (upper panels) and 3 μm (lower panels). (**C** to **E**) Representative images of TEM of OVCAR-5 cells. Black arrowheads indicate the disrupted nuclear envelop of MN. Scale bars, 2 μm (C) and 500 nm (D and E). (**F**) Serial confocal images of OVCAR-5 cells. Nuclei were stained with DAPI. IF staining for Lamin A/C and EEA1 was performed with antibodies as described in Materials and Methods. Scale bars, 5 μm (upper panel) and 2.5 μm (lower panel). (**G**) Western blot of OVCAR-5 cells with CD63 knockdown (CD63 KD). CTRL indicates the OVCAR-5 cells transfected with a scramble shRNA sequence. Densitometry analysis is quantified in the bar chart. (**H**) Representative images of exosome from CD63-knockdown OVCAR-5 cells in imaging flow cytometry analysis. The fold change of nExo population. The experiment was performed in three independent biological replicates, and the average of fold changes was calculated. Error bars represent SD. Statistical significance was determined by conducting an unpaired Student's *t* test. (**I**) The samples of OVCAR-5 cells with IP experiments for CD63 were analyzed with 2% agarose gel electrophoresis, and DNAs were visualized by ethidium bromide staining. (**J**) Western blot of OVCAR-5 cells with IP experiments for CD63. CTRL-IP indicates the OVCAR-5 cells treated with negative control immunoglobulin G (IgG) in the Universal Magnetic Co-IP Kit (54002, Active Motif).

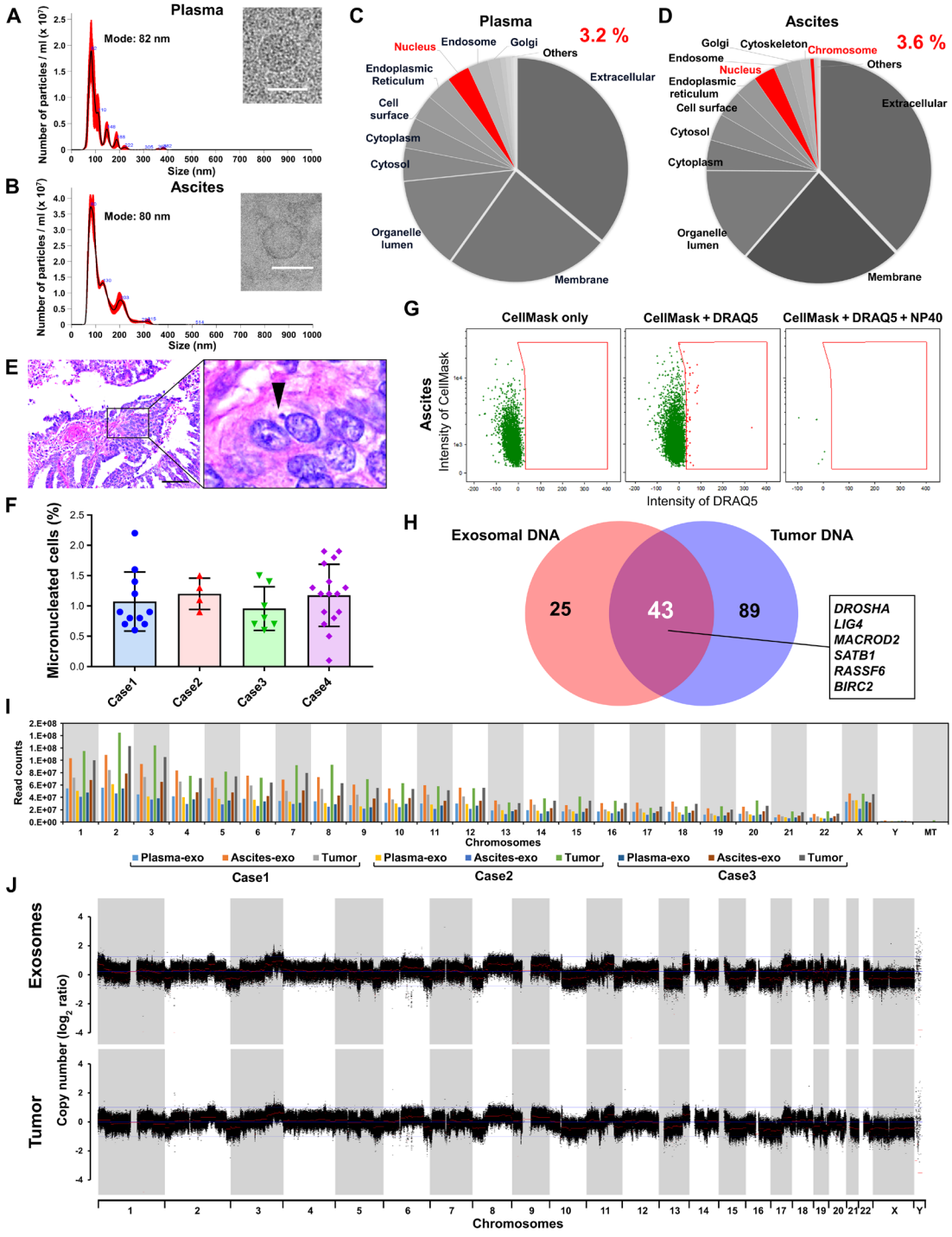

Fig. 6. Detection of nExo in clinical samples. (**A** and **B**) NTA for exosomes was derived from plasma and ascites from patients with high-grade serous ovarian carcinoma, along with representative cryo-EM images. Scale bars, 100 nm. (**C** and **D**) Pie charts of the cellular compartment of origin of proteins based on MS analysis from plasma- and ascites-derived exosomes. Nuclear components are highlighted in red. (C) "Others" includes cytoskeleton, mitochondrion, ribosome, and vacuole. (D) "Others" includes mitochondrion, nucleus, organelle lumen, ribosome, and vacuole. (**E**) Representative tissue image of high-grade serous ovarian carcinoma stained with H&E. Black arrowhead indicates MN. Scale bars, 100 μm. (**F**) Population of micronucleated cells in high-grade serous ovarian carcinoma tissue. Pretreated tissue slides were obtained and analyzed as described in Materials and Methods. Each dot indicates one view for analysis. $n = 4$. (**G**) Representative imaging flow cytometry images of exosomes obtained from ascites of patients with high-grade serous ovarian carcinoma. (**H**) Venn diagram showing overlapping exonic mutated genes between tumor and ascites exosomes. Samples were obtained from patients with HGSC. *DROSHA, LIG4, MACROD2, SATB1, RASSF6,* and *BIRC2* were included in the 43 overlapping genes. (**I**) Read counts of all chromosomes in plasma- and ascites-derived exosomal DNA and tumor DNA. All three cases were from patients with advanced-stage HGSC. (**J**) CNV status in gDNA in ascites-derived exosomal DNA and corresponding primary tumor from patients with HGSC. Profiles demonstrate somatic chromosomal gains (upper) and losses (lower), as well as normal polymorphisms.

nExo from human plasma and ascites samples contained gDNA, and this ratio was consistent with the in vivo mouse model data. On the basis of the finding that nontransformed cells release fewer nExos, this discrepancy between the proportions of in vitro and in vivo DNA-containing exosomes (around 10% and less than 1%, respectively) is not surprising; tumor-derived exosomes in biofluids are likely a subset of a much larger population of non–tumor cell–derived exosomes. Given the higher secretion of nExo by cancer cells, the presence and quantity of nExos could serve as a cancer biomarker. In addition, the gDNA in nExos can be interrogated for tumor-associated genetic alterations. Cell-free DNA (cfDNA) is a potential biomarker for cancer patients (*28*) and some studies suggest that a large proportion of plasma cfDNA is found within exosomes. Further research is required to understand the biological differences between cfDNA and nExos, which may be minimal due to the potential overlap between them.

Our findings suggest that genotoxic drugs induce MN formation and nExo release. In this study, we used topotecan and olaparib because of their direct effects on DNA repair mechanisms (*29*, *30*). Although both drugs have different mechanisms for targeting cancer cells, both can induce genomic instability and induce apoptosis. MN serve as a marker of genomic instability, and they form either by chromosome mis-segregation during mitosis or from direct insults to gDNA (*31*). Our in vivo mouse experiments revealed a trend toward an increased number of micronucleated cells in the topotecan-treated group, but this difference was not statistically significant, which may reflect the single dose of topotecan used for this experiment. In addition, we observed a significant increase in the concentration of nExos in the ascites of tumor-bearing mice, but not in the serum. This difference may be due to an insufficient dose of the drugs, a small sample size, or a larger fraction of tumor-derived exosomes in ascites compared to serum.

The observation that the nuclear envelope of MN is unstable and prone to collapse, exposing its contents to the cell cytoplasm, prompted the idea that this event allows nuclear content to be loaded into exosomes (*13*). As described in previous sections, tetraspanins play a role in shuffling content into MVBs, which eventually gives rise to the secreted exosomes (*3*). In this study, we observed that CD63 surrounds the MN envelope and loads nuclear contents into exosomes. The role of CD63 in exosome cargo loading is further supported by a recent finding that CD63 interacts with the RNA binding protein, Y-box protein I, to load miR-223 into exosomes (*32*). To our knowledge, CD63 does not contain a canonical DNA binding domain. For this reason, we hypothesize that CD63 may interact with DNA binding proteins, such as histones, to indirectly load gDNA into exosomes. The presence of a complex containing CD63–Histone H2B–gDNA in our experiments suggests that this could play an important role in the loading of DNA into exosomes, but elucidating the dynamics and all the players involved in this process requires additional work beyond the scope of this current study.

Despite the growing interest in exosome biology, little is known about the biological function of nExos. Recently, Takahashi *et al.* (*8*) reported that gDNA is present in exosomes and that inhibiting total exosome secretion promotes cell senescence by stimulating the cGAS/STING inflammatory pathway. In recipient cells, it was demonstrated that T cell–derived extracellular vesicles containing genomic and mitochondrial DNA induced antiviral responses via the cGAS/STING cytosolic DNA–sensing pathway in dendritic cells (*33*). In addition, it is known that MN can promote the activation of the cGAS/STING pathway, resulting in an inflammatory response in both senescent and cancer cells (*14*, *34*).

Chromosomal instability has been observed to correlate with tumor metastasis, and a recent report suggested that this may be mediated by a cytosolic DNA response (*34*). Inflammation is a key inducer of cancer progression by creating a nourishing tumor microenvironment (*35*). In this context, it is not surprising that the secretion of nuclear content by cancer cells via exosomes may promote metastasis by promoting a proinflammatory environment. Further research is required to fully elucidate the role of nExos in modulating the tumor microenvironment.

It has been reported that plasma-derived exosomal DNA does not fully represent tumor CNV status due to the low concentration of tumor-derived exosomes (*36*). Consistent with this observation, our data showed that plasma-derived exosomes did not carry enough gDNA to obtain WGS libraries of sufficient complexity for accurate detection of CNV or single-nucleotide variation (SNV) (Fig. 6I and fig. S6). However, our data demonstrate that ascites-derived exosomes represent tumor CNV status. It is possible that the plasma exosome libraries show lower depth of coverage than the ascites exosomes or tumor. Several mutations related to DNA repair were found in matched tumor and ascites exosome DNA. Exploring the role of these genes and their potential for prediction of sensitivity or resistance to poly(adenosine diphosphate–ribose) polymerase (PARP) inhibitors in ovarian cancer remains to be determined. These findings suggest that ascites nExos rather than serum nExo can be a reliable biomarker source to probe the tumor genome. This is particularly important in HGSC where distinct CNV signatures can serve as predictors of treatment response and ultimately clinical outcome (*37*). The ability to quickly isolate and probe ascites nExo CNV may allow clinicians to optimize therapy regimens without the direct biopsy of tumors. Future studies must be done to understand whether CNV in ascites nExo directly correlates with CNV responses in ovarian cancer tumors and affects patient clinical outcomes.

Overall, our study provides the foundation for understanding the cellular mechanisms of nuclear content loading into exosomes and their potential biological functions. Moreover, to translate these findings in the clinic, further validation is needed for the use of nExo as biomarkers of clinical response and outcomes. The use of the described imaging flow cytometry method can monitor changes of nExos from patients who are either resistant or sensitive to genotoxic drugs. This is particularly important for ovarian cancer patients given the recent U.S. Food and Drug Administration (FDA) approval of olaparib and other PARP inhibitors for this cancer type.

MATERIALS AND METHODS

Pan-cancer TCGA ploidy analysis

Ploidy data from TCGA samples were downloaded from the Pan-Cancer TCGA project (https://www.cell.com/pb-assets/consortium/pancanceratlas/pancani3/index.html; accessed 8 September 2016).

Cell lines and tissue culture

The human ovarian cancer cell lines were obtained from the American Type Culture Collection (ATCC) and the University of Texas MD Anderson Cancer Center Characterized Cell Line Core Facility. Cell lines were routinely identified via short tandem repeat DNA profiling carried out by the Characterized Cell Line Core Facility at MD Anderson. Primary FTE cells were a gift from J. Liu from the Department of Pathology at MD Anderson. For all cell lines, mycoplasma

testing was done using the ATCC PCR Universal Mycoplasma Detection Kit (30-1012K). OVCAR-8 cells were cultured in HyClone RPMI 1640 medium (SH30027.01, GE Healthcare Life Sciences) supplemented with 15% fetal bovine serum (FBS) (Sigma-Aldrich) and 0.2% gentamicin (50146970, Thermo Fisher Scientific). OVCAR-5 cells were cultured in Dulbecco's modified Eagle's medium (DMEM; 10-013-CV; Corning) supplemented with 10% FBS and 0.2% gentamicin. FTE cells were cultured in medium 199 with MCDB 105 (1:1) with 10% FBS and 0.2% gentamicin. All cells were grown in humidified incubators kept at 37°C with 5% CO_2.

Isolation of exosomes

The isolation method for exosomes that was used in this study followed the standard methods of the International Society of Extracellular Vesicles (*38*). Cell lines described above were grown in the corresponding medium described above until 60 to 70% confluence was achieved. Cells were then washed twice with phosphate-buffered saline (PBS) and grown in corresponding medium containing 1% exosome-free FBS (EXO-FBS-250A-1, System Biosciences) plus 0.1% gentamicin for 48 hours. For exosome isolation, the harvested medium underwent serial centrifugation. First, the medium was spun down at 500*g* for 10 min to pellet any floating cells. Next, the supernatant was collected and spun down at 2000*g* for 30 min to pellet any residual cell debris. The resulting supernatant was then filtered through a 0.22-μm filter (SCGPU05RE and SLGP033RS, Millipore-Sigma) to remove any remaining large vesicles. After filtration, the medium was spun down at 40,000 rpm for 2 hours at 4°C in an ultracentrifuge (Optima XE, Beckman Coulter) with a Ti 45 fixed-angle rotor (339160, Beckman Coulter). The resulting exosome pellet was resuspended in 2 ml of PBS and then spun again at 40,000 rpm for 2 hours at 4°C. The final pellet was resuspended in PBS and stored at 4°C. Exosome concentration and quantity were determined using NTA with a NanoSight NS300 instrument (Malvern Panalytical).

Isolation and purification of exosomes from patient serum and plasma

To isolate exosomes from serum and ascites obtained from patients with ovarian cancer, 200 μl of each patient's serum or ascites sample was collected and stored at 4°C. The serum was diluted with an equal volume of PBS and then centrifuged at 2000*g* for 30 min at 4°C. The supernatant was transferred to clean tubes without disturbing the pellet and centrifuged at 12,000*g* for 45 min at 4°C. The supernatant was then transferred to fresh tubes and diluted with a large volume of PBS (about 3 ml). After filtration with a 0.22-μm filter, the supernatant was transferred to ultracentrifuge tubes and ultracentrifuged at 40,000 rpm for 2 hours at 4°C as described above. The supernatant was then discarded, and the exosome pellet was resuspended in 3 ml of PBS. This was followed by another 40,000 rpm ultracentrifugation spin for 70 min at 4°C. The final pellet was resuspended in PBS. To further purify patient-derived exosomes from abundant protein aggregates present in both serum and ascites, we used size exclusion chromatography as described previously (21). Exosome-enriched fractions were identified by both NTA and SDS–polyacrylamide gel electrophoresis (SDS-PAGE) methods (fig. S5, A to D).

Exosome staining for imaging flow cytometry and analysis

For quantitative analysis and imaging flow cytometry of exosomes, we adapted the method described by Erdbrugger *et al.* (16) using an Amnis ImageStream^X MarkII analyzer. Briefly, 3×10^9 to 5×10^9 particles were isolated from either tissue culture cells, mouse serum and ascites, or serum obtained from patients with ovarian cancer and resuspended in PBS. Exosomes were placed in a sterile 1.5-ml Eppendorf tube and stained with CellMask Green Plasma Membrane (CMG) stain (1:250 dilution; C37608, Thermo Fisher Scientific) for 30 min at 37°C, protected from light. Exosomes were then washed to remove excess CMG by adding 2 ml of PBS and pelleted by ultracentrifugation at 40,000 rpm for 2 hours at 4°C. The supernatant was discarded, and the exosome pellet was gently resuspended in 100 to 150 μl of PBS. For antibody staining of exosomes, CMG-stained exosomes were incubated with fluorophore-conjugated primary antibodies described below for 1 hour with gentle agitation at room temperature (RT), protected from light. After 1 hour, the exosomes were washed by placing them in 2 ml of PBS and pelleting them by ultracentrifugation at 40,000 rpm for 2 hours at 4°C. The resulting pellet was then resuspended in 100 to 150 μl of PBS.

To stain for dsDNA, CMG-stained exosomes were costained with DRAQ5 (62254, Thermo Fisher Scientific) at either 1:50 dilution for biofluid exosome samples or 1:250 dilution for cell culture samples and were lightly agitated at RT for 1 hour, protected from light. Samples were then placed on ice, and images of single exosomes were detected using the 60× objective of an Amnis ImageStream^X MarkII analyzer. The ImageStream was equipped with five lasers [200 mW 405 nm, 100 mW 488 nm, 200 mW 561 nm, 150 mW 642 nm, 70 mW 785 nm (SSC)], and all lasers were used at maximum power with the instrument set for 7 μm core diameter (low speed). Particle size was estimated using Invitrogen Flow Cytometry Sub-micron Particle Size Reference Beads (F13839, Thermo Fisher Scientific), allowing exclusion of particles <150 nm based on the signal detected from side scatter. Controls for all exosome analyses included detergent lysis controls, buffer controls without exosomes, reagents alone in buffer, and antibody-unstained samples. For detergent lysis controls, samples were incubated for 30 min at RT after adding the nonionic detergent NP-40 to a final concentration of 0.5%. All analyses, including gate placement and batch processing, were performed using the Amnis proprietary IDEAS and INSPIRE software packages at the South Campus Flow Cytometry and Cell Sorting Core, the University of Texas MD Anderson Cancer Center Flow Cytometry and Cellular Imaging Core Facility.

Antibodies included the CD9 V450 mouse anti-human (1:100; 561326, BD Biosciences), Nesprin-2 (1:100; MA5-18075, Thermo Fisher Scientific) conjugated to Alexa 594, Lamin A/C 636 (SC-7292, Santa Cruz Biotechnology) conjugated to Alexa 594, Lamin B1 (1:100; 8982, Abcam), and Importin (1:100; ab2811, Abcam) conjugated to Alexa 594. Conjugation of antibodies for Nesprin-2, LaminB1, and importin to Alexa fluorophores was performed by using the Molecular Probes Antibody Labeling Kit (A20185 and A20181, Thermo Fisher Scientific).

IF experiments and MN quantification

Cells were plated at a density of 5×10^4 cells on sterile, 0.17-mm-thick coverslips (12-548-A, Thermo Fisher Scientific) placed at the bottom of six-well plates. The next day, cells were treated for 24 hours with either vehicle control dimethyl sulfoxide (DMSO; 1:1000 dilution; D2650, Sigma-Aldrich), 20 μM olaparib (O-9201, LC Laboratories), or 10 nM topotecan (T2705-50MG, Sigma-Aldrich). After 24 hours, the cells were washed with PBS and refed with the appropriate cell culture medium to grow for another 48 hours, for a total time of 72 hours after initial plating on the coverslips.

The drug-treated cells were first washed three times with PBS, fixed with 4% paraformaldehyde (PFA; 50-980-487, Thermo Fisher Scientific) diluted in PBS, and incubated at RT for 15 min with light rocking. The PFA was discarded, cells were washed three times with PBS, and then incubated for 10 min at RT with 30 mM glycine (BP381-5, Thermo Fisher Scientific) diluted in PBS to quench any residual PFA. Next, the cells were washed three times with PBS and incubated with 0.2% Triton X-100 (BP151-500, Thermo Fisher Scientific) diluted in PBS for 10 min at RT with light shaking. Triton was discarded, and cells were placed in blocking buffer (10% goat serum and 1% bovine serum albumin in PBS, syringe-filtered with 0.22-μm filter) for 1 hour at 4°C. Cells were next incubated overnight at 4°C with Lamin A/C (1:1000; ab26300, Abcam and 1:200; sc-5275, Santa Cruz Biotechnology), CD63 (1:1000; ab1318, Abcam), EEA1 (1:500; ab109110, Abcam), LAMP1 (1:100; ab108597, Abcam), and LC3B (1:200; ab64781, Abcam) antibodies diluted in blocking buffer. After primary antibody incubation, cells were washed three times with PBS and incubated with secondary antibodies Alexa Fluor 488 goat anti-mouse immunoglobulin G (IgG) (1:200; 115-545-003, Jackson ImmunoResearch) and Alexa Fluor 596 goat anti-rabbit (1:200; 111-586-047, Jackson ImmunoResearch) as well as DAPI (1:1000; D9542-1MG, Sigma-Aldrich) diluted in blocking buffer and incubated for 30 min at RT while protected from light. Last, cells on coverslips were then washed four times with PBS and mounted on slides using ProLong Diamond Antifade Mountant (P36961, Thermo Fisher Scientific) and imaged with a Leica fluorescence microscope (Leica DM4000 M LED; Leica Microsystems) or an Andor Revolution XDi WD Spinning Disk Confocal microscope. For MN quantification, we counted the number of MN in each 40× field using 10 fields per sample.

Confocal imaging

Cells were plated at a density of 2×10^4 cells onto glass coverslips in six-well plates, placed back into the incubator, and allowed to grow for 48 to 72 hours. The growth medium was removed, and the cells were washed once with PBS and subsequently fixed with 3.7% formaldehyde for 15 min at RT. Cells were then permeabilized with 0.1% Triton X-100 for 5 min, washed two times, and blocked with 10% normal goat serum for 1 hour at 37°C. Primary antibodies CD63 (ab1318, Abcam), CD9 (ab97999, Abcam), CD81 (ab35026, Abcam), and Lamin A (ab26300 and ab8980, Abcam) were diluted in 1% normal goat serum and applied for 2 hours at 37°C. Primary antibodies were removed, cells were washed three times for 5 min with PBS, and incubated with Alexa-conjugated secondary antibodies diluted in Dulbecco's PBS for 1 hour at 37°C. Secondary antibodies were removed, coverslips were washed three times for 5 min, and mounted onto glass slides using Vectashield Hardset with DAPI (H-1500, Vector Labs). Images were acquired using a Zeiss LSM 710 confocal microscope with a 63× objective.

Western blotting

For Western blotting, harvested cells and exosomes were lysed with radioimmunoprecipitation assay buffer (RIPA) [25 mM tris (pH 7.5), 150 mM NaCl, 0.1% SDS, 0.5% sodium deoxycholate, 1% Triton X-100] supplemented with single-use phosphatase and protease inhibitors (78442, Thermo Fisher Scientific). Protein concentration was determined using the Micro BCA Protein Assay Kit (23235, Thermo Fisher Scientific) according to the manufacturer's protocol. For all Western blots, we used 5 to 10 μg of total cell or exosome lysate diluted with 2× Laemmli sample buffer (1610737, Bio-Rad), which was loaded onto 10% SDS denaturing polyacrylamide gels. Protein was transferred to a nitrocellulose membrane, blocked with 5% nonfat dry milk (AB10109-01000, AmericanBio) in tris-buffered saline with 0.1% Tween 20 (TBS-T) for 1 hour at RT, and incubated with the indicated antibodies diluted in 5% milk in TBS-T overnight at 4°C with light agitation. The next day, the membrane was washed three times with TBS-T for 10 min with light agitation. After the third wash, the membrane was incubated with species-specific secondary antibodies conjugated to horseradish peroxidase (NA931V and NA934V; GE Healthcare) and diluted 1:2500 in 5% milk in TBS-T for 1 hour at RT with light agitation. The membrane was then washed three times in TBS-T and finally developed using Western Lightning Plus ECL (NEL105001EA; PerkinElmer) on x-ray film (F-BX57, Phenix). For reprobing of Western blots, membranes were stripped with Restore PLUS Western Blot Stripping Buffer (46430, Thermo Fisher Scientific), reblocked in 5% milk TBS-T, and incubated with primary antibody. In this study, we used the following primary antibodies and dilutions: CD63 (1:3000; EXOAB-CD63A-1, System Biosciences), TSG101 (1:500; ab30871, Abcam), Alix (1:500; SC-53538, Santa Cruz Biotechnology), GRP94 (1:500; SC-393402, Santa Cruz Biotechnology), Lamin A (1:1000; ab26300, Abcam), and Histone H2B (1:500; ab1790, Abcam).

Plasmid transfections

For transient transfection of cells for live cell imaging, we used a method that was similar to the one described above with some modifications. Briefly, cells were plated at a density of 3×10^5 to 4×10^5 cells per six-well plate so that cells reached 90% confluence the next day. For transfections, Lipofectamine 2000 (11668500, Thermo Fisher Scientific) was complexed with 1 μg of the plasmid mEmerald-CD9-10 (54029, Addgene), as described above. At 48 hours after transfection, mEmerald-CD9 expression was verified by using fluorescent microscopy, and cells were used for subsequent live cell imaging experiments.

Cloning of mCherry-LaminA/C into a lentiviral vector

The mCherry-LaminA/C fusion protein was cloned from the parental plasmid mCherry-LaminA-C-18 (55068, Addgene) using restriction enzyme digestion with Nhe I (FD0973, Thermo Fisher Scientific) and Bam HI (FD0054, Thermo Fisher Scientific). The parental lentiviral vector pCDH-CMV-MCS-EF1α-Puro (CD510B-1, System Biosciences) was also digested with Nhe I and Bam HI. One microgram of each parental plasmid was used for the restriction enzyme digestions. Digestion products were run on a 1% agarose gel made with 1× TBE buffer (1.0 M tris, 0.9 M boric acid, and 0.01 M EDTA; 15581-028, Invitrogen UltraPure). The desired digestion products were cut and gel-purified using the GeneJET Gel Extraction Kit (K0692, Thermo Fisher Scientific) according to the manufacturer's protocol. mCherry-LaminA/C was ligated into pCDH-CMV-MCS-EF1α-Puro using T4 ligase (M0202S, NEB) for 12 hours at 16°C according to the manufacturer's protocol. The ligation product was transformed into NEB Stable Competent *Escherichia coli* (C3040I, NEB) according to the NEB protocol, plated on ampicillin plates, and grown at 37°C for 12 hours. Colonies were picked and grown in LB medium at 37°C (12795027, Thermo Fisher Scientific) supplemented with ampicillin (BP1760-5, Fisher BioReagents). Plasmid DNA was purified using the Qiagen Plasmid Plus Midi Kit (12945) according to the manufacturer's protocol.

Lentiviral production and cell transduction

For lentiviral production, human embryonic kidney (HEK) 293T cells (grown in DMEM, 10% FBS, and 0.2% gentamicin) were transfected using Lipofectamine 2000 (11668500, Thermo Fisher Scientific) with 10 μg of lentiviral plasmid (see below for plasmids used), along with 5 μg of psPAX2 (12260, Addgene) and 2.5 μg of pMD2.G (12259, Addgene) lentiviral helper plasmids. Cell medium containing newly generated virus was collected 48 and 72 hours after transfection, pooled, centrifuged to clear any cell debris, and syringe-filtered using a 0.45-μm filter (190-2545, Thermo Fisher Scientific). For infection, cells were plated at 50% confluence in six-well plates and incubated with 2 ml of newly produced virus along with polybrene at a 1:1000 dilution (sc-134220, Santa Cruz Biotechnology) for 24 hours. Cells were then refed with regular medium and allowed to grow. The cells with vectors containing drug selection markers such as puromycin (A11138-03, Gibco) were exposed to puromycin for 48 hours after initial lentiviral infection. Surviving cells were expanded and used for subsequent in vitro and in vivo experiments. Lentiviral vectors used in this study included pCDH-CMV-MCS-EF1α-Puro-mCherry-LaminA/C (see previous section), pCT-CD63-GFP (CYTO120-VA-1, System Biosciences), pLenti6-H2B-mCherry (89766, Addgene), and pLKO-CD63shRNA (SHCLNV-NM_001780, Sigma-Aldrich). For shRNA sequences, two different target sequences for human *CD63* were used: (i) 5′-CCGGGCCTCGTGAAGAGTATCAGAACTC-GAGTTCTGATACTCTTCACGAGGCTTTTT-3′ and (ii) 5′-CCG-GGCAAGGAGAACTATTGTCTTACTCGAGTAAGA-CAATAGTTCTCCTTGCTTTTT-3′. The nontargeting shControl 5′-CCGGCCTAAGGTTAAGTCGCCCTCGCTCGAGCGAGGG-CGACTTAACCTTAGGTTTTTG-3′ was used.

Luciferase labeling of OVCAR-5 cells

To label cells with luciferase for in vivo imaging system (IVIS) imaging, cells were infected with the lentiviral vector pGreenFire1-CMV (TR011PA-1, System Biosciences), which coexpresses green fluorescent protein (GFP). Cells were sorted using FACSAria IIIu at the South Campus Flow Cytometry and Cell Sorting Core, MD Anderson Flow Cytometry and Cellular Imaging Core Facility for GFP positivity.

In vivo experiments

For the in vivo mouse experiments, female athymic (NCr-nude) mice were purchased from Taconic Biosciences. Mice were cared for in accordance with the American Association for Assessment and Accreditation of Laboratory Animal Care and the U.S. Public Health Service policy on Humane Care and Use of Laboratory Animals. All studies and experiments that were performed were supervised and approved by the MD Anderson Institutional Animal Care and Use Committee. Mice were 10 to 15 weeks old at the time of tumor intraperitoneal cell injections. OVCAR-5 luciferase–labeled cells (1×10^6) were injected intraperitoneally into each mouse.

Injected cells were first grown in the indicated medium until they reached 70% confluence. The cells were then trypsinized (SH30042.01, GE Healthcare), washed twice with PBS, and resuspended in ice-cold Hanks' balanced salt solution (21-021-CV; Cellgro). To determine tumor cell uptake, mice were injected with 200 μl of luciferin (14.7 mg/ml) (LUCK-1G; GoldBio) and imaged using IVIS. Non–tumor-bearing mice were removed from the experiment. Mice were randomly assigned to the treatment groups. We conducted all in vivo experiments, and the primary investigator was not blinded to the allocation of each treatment group. At the end of the experiment, blood and ascites were collected from each tumor-bearing mouse, and exosomes were isolated.

Enrichment of MN fractions

Methods for isolation and purification of cultured cell MN were adapted from Damaraju *et al.* (*19*) with the following modifications: Harvested OVCAR-5 cells were scraped from 15-cm tissue cultures using ice-cold PBS supplemented with protease and phosphatase inhibitors and pelleted by centrifugation at 500*g* for 10 min at 4°C. The supernatant was carefully discarded, and the cell pellet was gently resuspended in 1 ml of ice-cold cell lysis buffer obtained from the Active Motif ChIP-IT Express Chromatin Immunoprecipitation Kit supplemented with protease and phosphatase inhibitors provided by the kit (53008, Active Motif). Cells were incubated in lysis buffer on ice for 30 min and then carefully pipetted into a 1-ml Dounce homogenizer. We used 20 to 25 strokes in the Dounce homogenizer to release intact cell nuclei from the rest of the cell components. To ensure successful cell lysis, a small aliquot of the cell suspension was stained with DAPI (1:1000) and imaged with our fluorescence microscope (Fig. 4A). Lysed cells were then spun at 2400*g* at 4°C to pellet cell nuclei. Supernatant from this step, which contained MN, was kept, and pelleted cell nuclei were discarded. Cell supernatant was loaded to a sucrose gradient (84097-1KG, Sigma-Aldrich) prepared in PBS by using fractions indicated by Damaraju *et al.* (*19*). The fraction corresponding to 25% sucrose was collected and mixed with an equal volume of ice-cold PBS. The fraction was centrifuged at 13,500*g* at 4°C to pellet the MN, the supernatant was discarded, and MN were resuspended in ice-cold PBS with protease and phosphatase inhibitors. To confirm the presence of MN, an aliquot of the suspension was stained with DAPI and analyzed with a fluorescence microscope (Fig. 3A). The purified fraction was either sent for MS analysis or stored at −80°C.

Immunoprecipitation experiments

For IP analysis, whole-cell lysates were extracted following the manufacturer's protocol provided by the Universal Magnetic Co-IP Kit (54002, Active Motif), and 1000 μg of protein was immunoprecipitated using 2.5 μg of antibody. The prepared samples were used for Western blot and DNA staining by agarose gel electrophoresis.

DNase I treatment

Samples were treated with DNase I (1 unit/μl; E1011-A, Zymo Research) with DNase digestion buffer (E1011-1-4, Zymo Research) and incubated at 37°C for 45 min. Subsequently, 5 μl of EDTA solution (1861274, Thermo Fisher Scientific) was added, and the samples were heated at 65°C for 5 min.

Human tumor samples and MN quantification

High-grade ovarian tumor samples were obtained from MD Anderson Tissue Bank under an approved institutional review board protocol, and written consent was obtained for the use of patient samples for research. The details regarding the quality control for the samples obtained from CHTN can be found at https://www.chtn.org/quality.html. For MN identification and quantification, the Vectra Polaris platform (PerkinElmer) was used, and inForm software (PerkinElmer) was used to systematically count MN. After tissue segmentation, a number of nuclei in views were calculated by the cell segmentation process, and MN was defined as over 0.85 roundness and less than approximately 3 μm size (95 pixels in 96 dpi images), as shown in Fig. 3D.

Time-lapse cell imaging

Fluorescently labeled cells were plated onto sterilized four-chamber 0.170-mm glass-bottom slides (80427, Ibidi) at a density of 1×10^4 cells per well. The following day, cells were imaged with an Andor Revolution XDi WD Spinning Disk Confocal microscope on a humidified stage, which was kept at 37°C with 5% CO_2 to simulate optimal growing conditions. Hepes (10 mM) (25-060-Cl; Corning) buffer was added to the culture medium before imaging to maintain a stable pH throughout imaging. Cells were imaged every 5 min for movie S1 and every 10 min for movie S2 using a 63× silicon immersion objective lens for 12 hours. Images and movies were analyzed with Imaris Image Analysis Software (Bitplane, Oxford Instruments). For labeling of cell membranes, CellMask Deep Red (C10046, Thermo Fisher Scientific) was used according to the manufacturer's protocol.

Electron microscopy

Cells were prepared in the following manner: 2.5×10^4 OVCAR-5 cells were plated on plastic 24-well tissue culture plates. Forty-eight hours later, cells were washed three times with PBS and fixed with 4% PFA with 0.1% of glutaraldehyde (G7651-10ML, Sigma-Aldrich) diluted in PBS, which was 0.22 μm syringe-filtered for 15 min at RT. Cells were then washed three times with PBS, and 2% glutaraldehyde was added to each well of cells. Twenty-four–well plate was then kept at 4°C until ready for TEM processing at the MD Anderson Cancer Center High Resolution Electron Microscopy Facility. Samples were fixed with a solution containing 3% glutaraldehyde plus 2% PFA in 0.1 M cacodylate buffer (pH 7.3), then washed in 0.1 M sodium cacodylate buffer and treated with 0.1% Millipore-filtered cacodylate-buffered tannic acid, postfixed with 1% buffered osmium, and stained en bloc with 1% Millipore-filtered uranyl acetate. The samples were dehydrated in increasing concentrations of ethanol and then infiltrated with and embedded in LX-112 resin. The samples were polymerized in a 60°C oven for approximately 72 hours. Ultrathin sections were cut in a Leica Ultracut microtome (Leica, Deerfield, IL), stained with uranyl acetate and lead citrate in a Leica EM stainer, and examined in a JEM 1010 transmission electron microscope (JEOL, USA Inc., Peabody, MA) at an accelerating voltage of 80 kV. Digital images were obtained using the AMT Imaging System (Advanced Microscopy Techniques Corp., Danvers, MA).

For cryo-EM, 1×10^{10} to 5×10^{10} exosomes were isolated from either ovarian cancer cells or patient plasma and ascites and resuspended in 50 μl of PBS. The samples were prepared for cryo-EM studies at the Baylor College of Medicine Cryo-Electron Microscopy Core Facility (BCM, Houston, TX). The grids (Quantifoil R2/1, Cu 200 mesh) were pretreated with a 45-s air-glow discharge immediately before vitrification. During vitrification, 3 μl of exosome sample was applied to a grid, blotted for 4 s, and subsequently plunged into liquid ethane using Vitrobot Mark IV (FEI Company, Hillsboro, OR) set at RT and 100% humidity. The frozen grids were then imaged using a JEOL 2200FS microscope (JEOL) fitted with a post-column energy filter with a width of 30 eV. Before imaging, the microscope was carefully aligned to prevent any column-based distortion or astigmatism that can occur. Images were collected at magnifications of 25,000× and 40,000× with respective pixel sizes of 2.51 and 1.64 Å using a DE-20 camera (Direct Electron, San Diego, CA). Imaging was done with a dose rate of ~30e−/Å2/s using a 1-s exposure time with a capture rate of 24 frames/s. Gain and dark corrections were applied automatically to produce the final images used.

MS analysis

A total of about 20 to 40 μg of intact isolated exosomes from either OVCAR-5 cells or patient samples in addition to 40 μg of OVCAR-5 were quantified using the Micro BCA Protein Assay Kit (23235, Thermo Fisher Scientific) and sent to the MD Anderson Mass Spectrometry core. Proteins were acetone-precipitated (5:1) overnight at −20°C and digested with 200 to 500 ng of modified trypsin (sequencing grade; Promega, Madison, WI) in the presence of RapiGest (Waters, Milford, MA) for 18 hours at 37°C. The resulting peptides were analyzed by high-sensitivity liquid chromatography–MS/MS on an Orbitrap-Fusion mass spectrometer (Thermo Fisher Scientific, Waltham, MA). Proteins were identified by searching the fragment spectra in the SwissProt (EBI) protein database using Mascot (version 2.6.2; Matrix Science, London, UK). Typical search settings were mass tolerances: 10 ppm (parts per million) precursor, 0.8d fragments; variable modifications, methionine sulfoxide, pyro-glutamate formation; up to two missed cleavages. False discovery rate estimates were from Proteome Discoverer (version 2.2, Thermo Fisher Scientific).

Library preparation and sequencing

Exosome DNA was isolated from 1×10^{10} to 5×10^{10} exosomes from either tissue culture cells or bodily fluids with the System Biosciences XCF Exosomal DNA Isolation Kit (XCF200A-1, Systems Biosciences) following the manufacturer's protocol. gDNA from either cultured cells or tumor tissue was isolated using the Qiagen DNeasy Blood and Tissue Kit (69506, Qiagen) according to the manufacturer's protocol. DNA concentration was determined using both the NanoDrop 2000 Spectrophotometer (Thermo Fisher Scientific) and the Agilent 2100 Bioanalyzer Kit (5067-150, Agilent Technologies) following the manufacturer's protocol.

WGS next-generation sequencing (NGS) libraries were constructed either using the KAPA HyperPlus Kit (Roche Holding AG) or the Zymo Pico Methyl-Seq Kit (Zymo Research), depending on the source of the DNA sample. The KAPA kit provides a relatively unbiased enzymatic fragmentation method, which allows balanced coverage and low-input polymerase chain reaction (PCR)–free DNA NGS library construction (*39*). dsDNA (Onco-NoPCR) (300 ng) in 0.5 mM EDTA was added with the appropriate amount of conditioning solution to the enzymatic fragmentation step. The dsDNA was then incubated with the fragmentation enzyme for 6 min at 37°C. The fragmented samples were then end-repaired and A-tailed, and Illumina-indexed adapters were ligated onto the ends of the dsDNA. A two-sided AmpureXP bead selection protocol (0.55×/0.8× /2.5×) was used to select for an average NGS library size of approximately 481 base pairs (bp).

The Zymo kit protocol is a post-bisulfite adapter tagging NGS library protocol and is relatively unbiased as a hybridization-based NGS library generation method. This protocol was modified to exclude the bisulfite DNA fragmentation step, extend the initial adapter tagging extension step from 8 to 30 min, and extend the two PCR extension steps from 1 to 6 min. ExDNA (extracellular DNA) (100 ng) was used to generate a NGS library with this Zymo kit. Six cycles of PCR were used during the final index adapter addition step. A two-sided AmpureXP bead selection protocol (0.55×/0.8× /1.2×) was used to select for an average NGS library size of approximately 473 bp.

The NGS libraries were quantified using a PicoGreen-based assay (Qubit, Thermo Fisher Scientific), and for quality control purposes,

their size distribution profiles were determined using a Bioanalyzer instrument (Agilent Technologies Inc.) The NGS libraries were then sequenced on a NovaSeq 6000 instrument (Illumina, San Diego, CA) using paired-end 2 × 150–bp reads (UCSF Functional Genomics Core, University of California, San Francisco, San Francisco, CA) or a HiSeq 4000 instrument (Illumina, San Diego, CA) using paired-end 2 × 100–bp reads (IGM Genomics Center, University of California, San Diego, La Jolla, CA).

Bioinformatics analysis

Regarding cell line samples, the fastq files were first quality-controlled using FastQC (version 0.11.4) and adapters were trimmed using Trim Galore (version 0.4.1). The trimmed fastq files were then mapped to GRCh38 (GCA_000001405.15) using Bowtie2 (version 2.2.7) (*40*) and duplicated, sorted, and indexed using Samtools (version 1.3). The OncoNoPCR sample was sequenced to an average depth of 23×, and the ExDNA was sequenced to an average depth of 20×. Copy number alterations were called using cnvkit-0.9.6a0-py27_2. The batch WGS method was used after calculating the sequence-accessible coordinates from the reference genome. CNVs were then called using the following command: cnvkit.py batch --method wgs *sort.bam -n –f ../GCA_000001405.15_GRCh38_no_alt_analysis_set.fna --access access-excludes.GRCh38.bed --output-reference my_flat_reference.cnn -p 12 --scatter --diagram -d cnv_data/. Adjacent regions with the same copy number calls were merged using the cnvkit.py call –filter option. Copy number alterations were considered to be overlapping if they contained at least a 30% reciprocal overlap using Bedtools (version 2.25.0). Figures were made using cnvkit's scatter function and circos-0.69-3.

Regarding clinical samples, fastq files are aligned to the reference genome (human Hg19) using Burrows-Wheeler Alignment tool (BWA) with three mismatches, with two in the first 40 seed regions for sequences less than 100 bp. The aligned BAM files are subjected to mark duplication, realignment, and recalibration using Picard and GATK before any downstream analyses. Somatic mutations were called using MuTect, and indels were called using Pindel. DNA copy number analysis is conducted using HMMcopy following circular binary segmentation (CBS). DNA from blood cells was used as the reference in all of the above analyses. Mutation and indel calls were filtered using thresholds of ≥20 reads covering the called event for plasma, ascites, or tumor tissues and ≥20 reads for blood cells. An allele frequency cutoff of 0.2 was also applied to the mutation and indel data.

Statistical analysis

All statistical analyses of in vitro and in vivo experiments were done using GraphPad Prism 7 and the SPSS software program (version 24.0, IBM Corporation). To determine whether differences between the two groups were significant, we used a two-tailed Student's *t* test (equal variance). For these analyses, a *P* value of <0.05 was considered statistically significant. Results were presented as the mean ± SD.

SUPPLEMENTARY MATERIALS

Supplementary material for this article is available at http://advances.sciencemag.org/cgi/content/full/5/11/eaax8849/DC1

Fig. S1. Optimization of imaging flow cytometry analyses for exosomes.
Fig. S2. Characterization of nExo.
Fig. S3. Analyses of cell MN and exosomes treated with genotoxic drugs.
Fig. S4. Imaging of MN in ovarian cancer cells.
Fig. S5. Characterization of nExo and MN in human samples.
Fig. S6. WGS for clinical samples.
Fig. S7. Proposed model for the mechanism underlying nExo synthesis.
Movie S1. Time-lapse imaging in mCherry-LaminA/C–expressing OVCAR-5 cells.
Movie S2. Time-lapse imaging in mCherry-Histone H2B–expressing OVCAR-5 cells.

View/request a protocol for this paper from *Bio-protocol*.

REFERENCES AND NOTES

1. C. Théry, L. Zitvogel, S. Amigorena, Exosomes: Composition, biogenesis and function. *Nat. Rev. Immunol.* **2**, 569–579 (2002).
2. G. Raposo, W. Stoorvogel, Extracellular vesicles: Exosomes, microvesicles, and friends. *J. Cell Biol.* **200**, 373–383 (2013).
3. M. S. Pols, J. Klumperman, Trafficking and function of the tetraspanin CD63. *Exp. Cell Res.* **315**, 1584–1592 (2009).
4. H. Valadi, K. Ekström, A. Bossios, M. Sjöstrand, J. J. Lee, J. O. Lötvall, Exosome-mediated transfer of mRNAs and microRNAs is a novel mechanism of genetic exchange between cells. *Nat. Cell Biol.* **9**, 654–659 (2007).
5. B. Mateescu, E. J. K. Kowal, B. W. M. van Balkom, S. Bartel, S. N. Bhattacharyya, E. I. Buzás, A. H. Buck, P. de Candia, F. W. N. Chow, S. Das, T. A. P. Driedonks, L. Fernández-Messina, F. Haderk, A. F. Hill, J. C. Jones, K. R. Van Keuren-Jensen, C. P. Lai, C. Lässer, I. di Liegro, T. R. Lunavat, M. J. Lorenowicz, S. L. N. Maas, I. Mäger, M. Mittelbrunn, S. Momma, K. Mukherjee, M. Nawaz, D. M. Pegtel, M. W. Pfaffl, R. M. Schiffelers, H. Tahara, C. Théry, J. P. Tosar, M. H. M. Wauben, K. W. Witwer, E. N. M. Nolte-'t Hoen, Obstacles and opportunities in the functional analysis of extracellular vesicle RNA—An ISEV position paper. *J. Extracell. Vesicles* **6**, 1286095 (2017).
6. N. Kosaka, Y. Yoshioka, Y. Fujita, T. Ochiya, Versatile roles of extracellular vesicles in cancer. *J. Clin. Invest.* **126**, 1163–1172 (2016).
7. L. Balaj, R. Lessard, L. Dai, Y.-J. Cho, S. L. Pomeroy, X. O. Breakefield, J. Skog, Tumour microvesicles contain retrotransposon elements and amplified oncogene sequences. *Nat. Commun.* **2**, 180 (2011).
8. A. Takahashi, R. Okada, K. Nagao, Y. Kawamata, A. Hanyu, S. Yoshimoto, M. Takasugi, S. Watanabe, M. T. Kanemaki, C. Obuse, E. Hara, Exosomes maintain cellular homeostasis by excreting harmful DNA from cells. *Nat. Commun.* **8**, 15287 (2017).
9. B. K. Thakur, H. Zhang, A. Becker, I. Matei, Y. Huang, B. Costa-Silva, Y. Zheng, A. Hoshino, H. Brazier, J. Xiang, C. Williams, R. Rodriguez-Barrueco, J. M. Silva, W. Zhang, S. Hearn, O. Elemento, N. Paknejad, K. Manova-Todorova, K. Welte, J. Bromberg, H. Peinado, D. Lyden, Double-stranded DNA in exosomes: A novel biomarker in cancer detection. *Cell Res.* **24**, 766–769 (2014).
10. M. Fenech, M. Kirsch-Volders, A. T. Natarajan, J. Surralles, J. W. Crott, J. Parry, H. Norppa, D. A. Eastmond, J. D. Tucker, P. Thomas, Molecular mechanisms of micronucleus, nucleoplasmic bridge and nuclear bud formation in mammalian and human cells. *Mutagenesis* **26**, 125–132 (2011).
11. K. Crasta, N. J. Ganem, R. Dagher, A. B. Lantermann, E. V. Ivanova, Y. Pan, L. Nezi, A. Protopopov, D. Chowdhury, D. Pellman, DNA breaks and chromosome pulverization from errors in mitosis. *Nature* **482**, 53–58 (2012).
12. M. Fenech, Cytokinesis-block micronucleus cytome assay. *Nat. Protoc.* **2**, 1084–1104 (2007).
13. E. M. Hatch, A. H. Fischer, T. J. Deerinck, M. W. Hetzer, Catastrophic nuclear envelope collapse in cancer cell micronuclei. *Cell* **154**, 47–60 (2013).
14. S. M. Harding, J. L. Benci, J. Irianto, D. E. Discher, A. J. Minn, R. A. Greenberg, Mitotic progression following DNA damage enables pattern recognition within micronuclei. *Nature* **548**, 466–470 (2017).
15. U. A. Matulonis, A. K. Sood, L. Fallowfield, B. E. Howitt, J. Sehouli, B. Y. Karlan, Ovarian cancer. *Nat. Rev. Dis. Primers.* **2**, 16061 (2016).
16. U. Erdbrugger, C. K. Rudy, M. E. Etter, K. A. Dryden, M. Yeager, A. L. Klibanov, J. Lannigan, Imaging flow cytometry elucidates limitations of microparticle analysis by conventional flow cytometry. *Cytometry A* **85**, 756–770 (2014).
17. A. Ng, N. Barker, Ovary and fimbrial stem cells: Biology, niche and cancer origins. *Nat. Rev. Mol. Cell Biol.* **16**, 625–638 (2015).
18. A. K. Mitra, D. A. Davis, S. Tomar, L. Roy, H. Gurler, J. Xie, D. D. Lantvit, H. Cardenas, F. Fang, Y. Liu, E. Loughran, J. Yang, M. Sharon Stack, R. E. Emerson, K. D. Cowden Dahl, M. V. Barbolina, K. P. Nephew, D. Matei, J. E. Burdette, In vivo tumor growth of high-grade serous ovarian cancer cell lines. *Gynecol. Oncol.* **138**, 372–377 (2015).
19. S. Damaraju, N. Zhang, N. Li, L. Tao, V. L. Damaraju, J. Dufour, C. Santos, X.-J. Sun, J. Mackey, D. S. Wishart, C. E. Cass, L. Li, Evidence for copurification of micronuclei in sucrose density gradient-enriched plasma membranes from cell lines. *Anal. Biochem.* **396**, 69–75 (2010).
20. D. K. Jeppesen, A. M. Fenix, J. L. Franklin, J. N. Higginbotham, Q. Zhang, L. J. Zimmerman, D. C. Liebler, J. Ping, Q. Liu, R. Evans, W. H. Fissell, J. G. Patton, L. H. Rome, D. T. Burnette, R. J. Coffey, Reassessment of exosome composition. *Cell* **177**, 428–445.e18 (2019).
21. A. N. Böing, E. van der Pol, A. E. Grootemaat, F. A. W. Coumans, A. Sturk, R. Nieuwland, Single-step isolation of extracellular vesicles by size-exclusion chromatography. *J. Extracell. Vesicles* **3**, 23430 (2014).

22. W.-T. Lu, B. R. Hawley, G. L. Skalka, R. A. Baldock, E. M. Smith, A. S. Bader, M. Malewicz, F. Z. Watts, A. Wilczynska, M. Bushell, Drosha drives the formation of DNA:RNA hybrids around DNA break sites to facilitate DNA repair. *Nat. Commun.* **9**, 532 (2018).
23. J. R. Chapman, M. R. G. Taylor, S. J. Boulton, Playing the end game: DNA double-strand break repair pathway choice. *Mol. Cell* **47**, 497–510 (2012).
24. A. Sakthianandeswaren, M. J. Parsons, D. Mouradov, O. M. Sieber, *MACROD2* deletions cause impaired PARP1 activity and chromosome instability in colorectal cancer. *Oncotarget* **9**, 33056–33058 (2018).
25. S. Kaur, Y. Coulombe, Z. M. Ramdzan, L. Leduy, J.-Y. Masson, A. Nepveu, Special AT-rich sequence-binding protein 1 (SATB1) functions as an accessory factor in base excision repair. *J. Biol. Chem.* **291**, 22769–22780 (2016).
26. H. Iwasa, T. Kudo, S. Maimaiti, M. Ikeda, J. Maruyama, K. Nakagawa, Y. Hata, The RASSF6 tumor suppressor protein regulates apoptosis and the cell cycle via MDM2 protein and p53 protein. *J. Biol. Chem.* **288**, 30320–30329 (2013).
27. B. Adamson, A. Smogorzewska, F. D. Sigoillot, R. W. King, S. J. Elledge, A genome-wide homologous recombination screen identifies the RNA-binding protein RBMX as a component of the DNA-damage response. *Nat. Cell Biol.* **14**, 318–328 (2012).
28. H. Schwarzenbach, D. S. B. Hoon, K. Pantel, Cell-free nucleic acids as biomarkers in cancer patients. *Nat. Rev. Cancer* **11**, 426–437 (2011).
29. G. J. Creemers, B. Lund, J. Verweij, Topoisomerase I inhibitors: Topotecan and irenotecan. *Cancer Treat. Rev.* **20**, 73–96 (1994).
30. B. G. Bitler, Z. L. Watson, L. J. Wheeler, K. Behbakht, PARP inhibitors: Clinical utility and possibilities of overcoming resistance. *Gynecol. Oncol.* **147**, 695–704 (2017).
31. G. C. Jagetia, T. K. Reddy, The grapefruit flavanone naringin protects against the radiation-induced genomic instability in the mice bone marrow: A micronucleus study. *Mutat. Res.* **519**, 37–48 (2002).
32. M. J. Shurtleff, M. M. Temoche-Diaz, K. V. Karfilis, S. Ri, R. Schekman, Y-box protein 1 is required to sort microRNAs into exosomes in cells and in a cell-free reaction. *eLife* **5**, e19276 (2016).
33. D. Torralba, F. Baixauli, C. Villarroya-Beltri, I. Fernández-Delgado, A. Latorre-Pellicer, R. Acín-Pérez, N. B. Martín-Cófreces, Á. L. Jaso-Tamame, S. Iborra, I. Jorge, G. González-Aseguinolaza, J. Garaude, M. Vicente-Manzanares, J. A. Enríquez, M. Mittelbrunn, F. Sánchez-Madrid, Priming of dendritic cells by DNA-containing extracellular vesicles from activated T cells through antigen-driven contacts. *Nat. Commun.* **9**, 2658 (2018).
34. S. F. Bakhoum, B. Ngo, A. M. Laughney, J.-A. Cavallo, C. J. Murphy, P. Ly, P. Shah, R. K. Sriram, T. B. K. Watkins, N. K. Taunk, M. Duran, C. Pauli, C. Shaw, K. Chadalavada, V. K. Rajasekhar, G. Genovese, S. Venkatesan, N. J. Birkbak, N. McGranahan, M. Lundquist, Q. LaPlant, J. H. Healey, O. Elemento, C. H. Chung, N. Y. Lee, M. Imielenski, G. Nanjangud, D. Pe'er, D. W. Cleveland, S. N. Powell, J. Lammerding, C. Swanton, L. C. Cantley, Chromosomal instability drives metastasis through a cytosolic DNA response. *Nature* **553**, 467–472 (2018).
35. G. Lorusso, C. Rüegg, The tumor microenvironment and its contribution to tumor evolution toward metastasis. *Histochem. Cell Biol.* **130**, 1091–1103 (2008).
36. C. Kahlert, S. A. Melo, A. Protopopov, J. Tang, S. Seth, M. Koch, J. Zhang, J. Weitz, L. Chin, A. Futreal, R. Kalluri, Identification of double-stranded genomic DNA spanning all chromosomes with mutated *KRAS* and *p53* DNA in the serum exosomes of patients with pancreatic cancer. *J. Biol. Chem.* **289**, 3869–3875 (2014).
37. G. Macintyre, T. E. Goranova, D. De Silva, D. Ennis, A. M. Piskorz, M. Eldridge, D. Sie, L.-A. Lewsley, A. Hanif, C. Wilson, S. Dowson, R. M. Glasspool, M. Lockley, E. Brockbank, A. Montes, A. Walther, S. Sundar, R. Edmondson, G. D. Hall, A. Clamp, C. Gourley, M. Hall, C. Fotopoulou, H. Gabra, J. Paul, A. Supernat, D. Millan, A. Hoyle, G. Bryson, C. Nourse, L. Mincarelli, L. N. Sanchez, B. Ylstra, M. Jimenez-Linan, L. Moore, O. Hofmann, F. Markowetz, I. A. McNeish, J. D. Brenton, Copy number signatures and mutational processes in ovarian carcinoma. *Nat. Genet.* **50**, 1262–1270 (2018).
38. K. W. Witwer, E. I. Buzás, L. T. Bemis, A. Bora, C. Lässer, J. Lötvall, E. N. Nolte-'t Hoen, M. G. Piper, S. Sivaraman, J. Skog, C. Théry, M. H. Wauben, F. Hochberg, Standardization of sample collection, isolation and analysis methods in extracellular vesicle research. *J. Extracell. Vesicles* **2**, 20360 (2013).
39. J. D. Ring, K. Sturk-Andreaggi, M. A. Peck, C. Marshall, A performance evaluation of Nextera XT and KAPA HyperPlus for rapid Illumina library preparation of long-range mitogenome amplicons. *Forensic Sci. Int. Genet.* **29**, 174–180 (2017).
40. B. Langmead, S. L. Salzberg, Fast gapped-read alignment with Bowtie 2. *Nat. Methods* **9**, 357–359 (2012).

Acknowledgments: We thank M. A. Chowdhury for help on the experiments regarding exosome isolation. We thank A. A. Haltom and N. B. Jennings for reviewing this manuscript. We also thank I. Forrester and H. Villarreal, the staff in the CryoEM Core at Baylor College of Medicine, for support on cryo-EM analyses. The Department of Scientific Publications at MD Anderson helped review this manuscript. **Funding:** Portions of this work were supported by the NIH (P30 CA016672, UH3TR000943, P50 CA217685, P50 CA098258, and R35 CA209904), MD Anderson Cancer Center Ovarian Cancer Moon Shot Program, the Blanton-Davis Ovarian Cancer Research Program, American Cancer Society Research Professor Award, Judy's Mission, and the Frank McGraw Memorial Chair in Cancer Research. We acknowledge members of the University of Texas MD Anderson Cancer Center cores including the South Campus Flow Cytometry and Cell Sorting Core; the Flow Cytometry and Cellular Imaging Facility; the High-Resolution Electron Microscopy Facility; the Characterized Cell Line Core Facility; the Research Histology, Pathology, and Imaging Core; and the Small Animal Imaging Facility Core. These shared resources are partially funded by NCI Cancer Support Grant P30CA16672. WGS was conducted at the IGM Genomics Center, University of California, San Diego, La Jolla, CA. This work used the Extreme Science and Engineering Discovery Environment (XSEDE), which is supported by National Science Foundation grant number ACI-1548562. This work used the XSEDE Comet at the San Diego Super Computer through allocation MCB140074. This work was also supported, in part, by Cancer Prevention Research Institute of Texas (CPRIT) grant number RP130397 and NIH grant number 1S10OD012304-01. A.Y. was supported by the Japan Society for the Promotion of Science (JSPS) Overseas Research Fellow and the Mochida Memorial Foundation for Medical and Pharmaceutical Research. A.Y. was also funded by the Foundation for Women's Cancer (Clovis Oncology Post-Doctoral Fellowship Award). A.V.-P. was supported by the NIH Partnership for Excellence in Cancer Research (U54CA096300/U54CA096297). **Author contributions:** A.Y. and A.V.-P. designed the study and performed almost all experiments, analyzed data, and wrote the manuscript. P.A.O., J.K.B., and T.J.O. performed parts of the imaging experiments. J.Z., X.S., P.D.H., R.M., and L.C.L. performed the sequencing experiments. J.L. prepared the cells for in vitro experiments and examined pathology samples. J.R. performed the statistical analyses on TCGA patient datasets. K.C.-D. supervised the imaging flow experiments. A.K.S. supervised the whole study and participated in manuscript preparation. All authors edited and approved the final manuscript. **Competing interests:** A.K.S. (consulting for Kiyatec and Merck, research funding from M-Trap, and stockholder in BioPath). The other authors declare that they have no competing interests. **Data and materials availability:** All data needed to evaluate the conclusions in the paper are present in the paper and/or the Supplementary Materials. Additional data related to this paper may be requested from the authors.

Submitted 1 May 2019
Accepted 24 September 2019
Published 20 November 2019
10.1126/sciadv.aax8849

Citation: A. Yokoi, A. Villar-Prados, P. A. Oliphint, J. Zhang, X. Song, P. De Hoff, R. Morey, J. Liu, J. Roszik, K. Clise-Dwyer, J. K. Burks, T. J. O'Halloran, L. C. Laurent, A. K. Sood, Mechanisms of nuclear content loading to exosomes. *Sci. Adv.* **5**, eaax8849 (2019).